RECONSTRUCTION ALGORITHMS FOR LIMITED ANGULAR DIFFRACTION TOMOGRAPHY

By

Pavel Roy Paladhi

A DISSERTATION

Submitted to
Michigan State University
in partial fulfillment of the requirements
for the degree of

Electrical Engineering—Doctor of Philosophy

2016

ABSTRACT

RECONSTRUCTION ALGORITHMS FOR LIMITED ANGULAR DIFFRACTION TOMOGRAPHY

By

Pavel Roy Paladhi

Tomography is a ubiquitous imaging modality applied to numerous fields like medical imaging, geophysical imaging, structural health monitoring etc. It is a process to view cross-sectional profile of an object or region of interest through solving an inverse problem. When diffracting sources are used as the interrogating energy, the specific tomographic reconstruction is termed 'Diffraction Tomography' as the algorithm accounts for diffraction effects. As a result, these algorithms are more complex than straight ray tomography algorithms viz. computed tomography which has been very successfully implemented for X-ray tomography, PET etc. Ideally, projection data covering full 360° around the region of interest is necessary for accurate reconstruction. However, in many practical applications, this is not always feasible. As a result, reconstruction is performed on limited datasets, essentially making the process a recovery from an under-determined system. This thesis focuses on development of novel and efficient methods to handle the challenges on limited data for image reconstruction under diffraction tomography. For a moderately limited coverage, some inherent redundancies in Diffraction Tomography projection data can be used to reduce the effect of limited coverage. For highly limited angular coverage, these redundancies are no longer available and cannot be exploited. Recently, however, optimization techniques involving l_1-norm minimization schemes under the so called 'compressed sensing' regime have shown promise. These algorithms are capable of almost exact

reconstruction of the object even with highly limited number of projections. This research has explored both techniques for moderate and highly limited angular tomography. In the first part of the thesis, for moderate angular access limitations, an optimum method for exploiting redundancy within projection data has been formulated. In the second part, for highly limited coverage with further limitations on the number of available projections, reconstruction schemes under compressed sensing regime have been examined. Further, this research demonstrates reconstruction of complex-valued objective function under the regime of compressed sensing. This generalizes the application of tomographic reconstruction for newer applications such as examining new complex structures (such as metamaterial and other smart material based structures) where knowledge of complex permittivity values is essential in evaluating structural integrity or morphological aberrations. The compressed sensing method heavily relies on sparsity of the reconstructed signal in some transformation domain. In this research, the sparsity has mainly been exploited through gradient magnitude of images. In a variety of applications, gradient magnitude of images are highly sparse, even if the images themselves are not. So the gradient magnitude of images can be effectively used as the sparse domain. Further, incorporation of multiple sparse domains into the compressed sensing framework has been explored. Using Haar wavelets in addition to gradient magnitude of images as the sparse domain has successfully been employed showing potential for significant improvements in image reconstruction from highly limited data through further research.

To all those who prepared me for this journey and were a part of this venture

ACKNOWLEDGMENTS

A PhD program is a challenging and rewarding journey. This thesis is a culmination of one such journey. It would not have come to fruition had it not been for the great family, teachers and friends I was so fortunate to have. This is a chance to express my thanks to all of them and the gratitude I feel to have them around me.

Special thanks and gratitude are due to my advisors Profs. Lalita and Satish Udpa as without their help this thesis would not have been possible. They have been great mentors, knowledgeable and eager to support my ideas; inspiring me to carry on, pulling me up during stressful times and having their continuous faith in me. Dr. Ashoke Sinha, Dept. of Statistics and Probability, MSU had been a great source of encouragement. His vision and mathematical insights were instrumental towards progress in multiple projects.

My grandparents and parents played a pivotal role in moulding my outlook and passion for education and research. To them I owe the core values I firmly believe in and which has helped me to surmount obstacles and remain on track. I am fortunate to have a great wife who has provided continuous support and inspired me to persevere against all odds by practising the same.

To my friends I made at MSU and those I have back at home, thanks for providing all the happy and memorable times and the support I got whenever needed, no questions asked.

Lastly, I should not forget to mention Michigan State University for providing me a great platform to learn, grow and evolve in my understanding of this world.

TABLE OF CONTENTS

LIST OF FIGURES ix

Part 1 Background 1

Chapter 1 Introduction 2

Chapter 2 Diffraction Tomography and Filtered Backpropagation technique 6
2.1 Introduction 6
2.2 The Helmholtz Equation 7
2.2.1 Born Approximation 11
2.2.2 Rytov Approximation 12
2.3 Fourier Diffraction Projection Theorem (FDPT) 13
2.4 Filtered Backpropagation Algorithm 14

Part 2 Accurate Reconstruction From Moderately Limited Projection Data 16

Chapter 3 Data Redundancy in Diffraction Tomography 17
3.1 Generation of Efficient Weight Functions 22

Chapter 4 Accurate Reconstructions for Moderately Limited Angular Measurements 29
4.1 Noiseless Reconstruction 29
4.2 Reconstruction with Noisy Data 33
4.3 Summary 37

Part 3 Reconstruction from highly limited projection data: Compressed sensing approach 40

Chapter 5 Overview 41
5.1 Background 41
5.2 CS Theory 43
5.2.1 Sparse Basis Representation 44
5.2.2 Sensing Matrix: The Restricted Isometry Property 47
5.2.2.1 Incoherent sampling 48
5.2.3 Image Reconstruction 50
5.2.3.1 l-2 Minimization 50
5.2.3.2 l-0 Minimization 51

5.2.3.3 l-1 Minimization . . . 52
5.2.3.4 Geometrical Insights . . . 53
5.2.3.5 Summary . . . 55

Chapter 6 CS based Reconstruction for DT . . . 56
6.1 Application of CS to sparse DT recovery . . . 57
6.2 Reconstruction . . . 59

Chapter 7 Reconstruction with Total Variation as l_1 penalty term . . . 60
7.1 Reconstruction with TV as l_1 minimizer . . . 62
7.1.1 Error Analysis . . . 64
7.1.2 Reconstruction from phantoms with realistic permittivity distribution 70
7.2 Multiple sparse domain incorporation . . . 73

Chapter 8 Conclusions . . . 80
8.1 Summary . . . 80
8.1.1 Exploiting data redundancy for moderately limited angular diffraction tomography . . . 81
8.1.2 Compressed Sensing based diffraction tomography from highly sparse data . . . 81
8.2 Contribution: Significance and Benefits . . . 82
8.3 Future Work . . . 84

APPENDICES . . . 86
Appendix A Distribution Function based weight generation . . . 87
Appendix B Non-linear Optimization Techniques . . . 89

BIBLIOGRAPHY . . . 98

LIST OF FIGURES

Figure 2.1: Classical scan configuration of 2D DT (left) and relation of scattered field data with the 2D Fourier space of the objective function (right). 14

Figure 3.1: (a) Fourier space coverage for 270° angular access by segment OB in fig.1 (b) same for segment OA of fig-1. (c) Superposition of the two coverages from (a) and (b). (d) The Fourier data-space in alternate co-ordinate system with angular coverage along y-axis and the frequency along x-axis. 19

Figure 3.2: Demonstration of the MS-FBPP concept (a) real part of original image, (b) FBPP reconstruction from 360° coverage (c) FBPP reconstruction from 270° coverage and (d) MS-FBPP reconstruction from 270° coverage 21

Figure 3.3: Demonstration of the MS-FBPP concept (a) imaginary part of original image, (b) FBPP reconstruction from 360° coverage (c) FBPP reconstruction from 270° coverage and (d) MS-FBPP reconstruction from 270° coverage 22

Figure 3.4: Beta-cdf plots for different values of the parameters a and b 25

Figure 3.5: Images showing weight distributions in Fourier domain generated by parametric variation of the beta-cdf (using the parameters shown in Fig. 3.4). Frequency is plotted along abscissa and angular coverage along ordinate. 26

Figure 3.6: Images showing weight distributions in Fourier domain generated by parametric variation of the beta-cdf. The parameters a and b used for each weight distribution are inset in each plot. Frequency is plotted along abscissa and angular coverage along ordinate. . . . 27

Figure 3.7: Corresponding reconstructions from using the weight distributions in Fig. 3.6 28

Figure 4.1: Reconstructed real part from complex test image under noiseless conditions. The left column shows reconstruction from 270° coverage and right column shows reconstruction from 200° coverage. (a)-(b) using regular FBPP, (c)-(d) using sine-sq weights, (e)-(f) using gamma-cdf weights, (g)-(h) using beta-cdf weights 30

Figure 4.2: Reconstructed imaginary part from complex test image under noiseless conditions. The left column shows reconstruction from 270° coverage and right column shows reconstruction from 200° coverage. (a)-(b) using regular FBPP, (c)-(d) using sine-sq weights, (e)-(f) using gamma-cdf weights, (g)-(h) using beta-cdf weights . . 31

Figure 4.3: Reconstruction of real part of image from 3dB awgn projection data using beta-cdf weights for angular coverages (a) 270° (b) 250° (c) 220° (d) 200° 34

Figure 4.4: Reconstruction of imaginary part of image from 3dB awgn projection data using beta-cdf weights for angular coverages (a) 270° (b) 250° (c) 220° (d) 200° 35

Figure 4.5: MAE calculated at different coverages for real part of reconstructed image with regular FBPP and MS-FBPP using different weights . 37

Figure 4.6: MAE calculated at different coverages for imaginary part of reconstructed image with regular FBPP and MS-FBPP using different weights 38

Figure 4.7: Percentage improvement of MAE from different weights over regular FBPP at different coverages for real part of reconstructed image 38

Figure 4.8: Percentage improvement of MAE from different weights over regular FBPP at different coverages for imaginary part of reconstructed image 39

Figure 5.1: (a) Sample image (b) zoomed-in view (c) Compressed image by retaining $< 5\%$ of largest coefficients in wavelet domain. (d)zoomed-in view of the compressed image 46

Figure 5.2: Visual interpretation of the effectiveness of different norms for signal recovery by minimization [1]: (a)A sparse vector s lies on a K-dimensional hyperplane aligned with the coordinate axes in R^N and so close to the axes (b) Recovery through l_2 minimization does not find the correct sparse solution on the translated nullspace (green hyperplane), but a non-sparse solution $\hat{s}$ with least energy. (c)With sufficient measurements, recovery by l_1 minimization does find the correct sparse solution s. 53

Figure 7.1: Reconstructions of real part of image with 45 views for different angular coverage of : (a) 180°, (b) 150°, (c) 120°, and (d) 90° . . 63

Figure 7.2: Reconstructions of imaginary part of image with 45 views for different angular coverage of : (a) 180°, (b) 150°, (c) 120°, and (d) 90° 63

Figure 7.3: Reconstructions of real part of image with 30 views for different angular coverage of : (a) 180°, (b) 150°, (c) 120°, and (d) 90° . . 65

Figure 7.4: Reconstructions of imaginary part of image with 30 views for different angular coverage of : (a) 180°, (b) 150°, (c) 120°, and (d) 90° 65

Figure 7.5: Reconstructions of real part of image with 20 views for different angular coverage of : (a) 180°, (b) 150°, (c) 120°, and (d) 90° . . 66

Figure 7.6: Reconstructions of imaginary part of image with 20 views for different angular coverage of : (a) 180°, (b) 150°, (c) 120°, and (d) 90° 66

Figure 7.7: Reconstructions of real part of image with 15 views for different angular coverage of : (a) 180°, (b) 150°, (c) 120°, and (d) 90° . . 67

Figure 7.8: Reconstructions of imaginary part of image with 15 views for different angular coverage of : (a) 180°, (b) 150°, (c) 120°, and (d) 90° 67

Figure 7.9: Percentage increase of MAE for real part of image as the coverage is lowered for a fixed number of projections. Graphs plotted for different number of projections 71

Figure 7.10: Percentage increase of MAE for imaginary part of image as the coverage is lowered for a fixed number of projections. Graphs plotted for different number of projections 71

Figure 7.11: Percentage increase of MAE for real part of image as the number of projections is lowered for a fixed coverage. Graphs plotted for different coverages 72

Figure 7.12: Percentage increase of MAE for imaginary part of image as the number of projections is lowered for a fixed coverage. Graphs plotted for different coverages 72

Figure 7.13: Reconstructions of real part of image with 15 views, when real and imaginary parts have similar physical boundaries, for different angular coverage of : (a) 180°, (b) 150°, (c) 120°, and (d) 90° . . 74

Figure 7.14: Reconstructions of real part of image with 15 views,when real and imaginary parts have similar physical boundaries, for different angular coverage of : (a) 180°, (b) 150°, (c) 120°, and (d) 90° . . . 74

Figure 7.15: Reconstructions of real part of image with 10 views, when real and imaginary parts have similar physical boundaries, for different angular coverage of : (a) 180°, (b) 150°, (c) 120°, and (d) 90° . . 75

Figure 7.16: Reconstructions of real part of image with 10 views,when real and imaginary parts have similar physical boundaries, for different angular coverage of : (a) 180°, (b) 150°, (c) 120°, and (d) 90° . . . 75

Figure 7.17: Reconstructions of real part of image with 15 views and 120° coverage, when real and imaginary parts have similar physical boundaries, for different noise levels (measured as % of mean signal energy level) : (a) 5%, (b) 10%, (c) 20%, and (d) 50% 76

Figure 7.18: Reconstructions of imaginary part of image with 15 views and 120° coverage, when real and imaginary parts have similar physical boundaries, for different noise levels (measured as % of mean signal energy level) : (a) 5%, (b) 10%, (c) 20%, and (d) 50% 76

Figure 7.19: Reconstructions of real part of image with 15 views, when real and imaginary parts have similar physical boundaries, for different angular coverage of : (a) 180°, (b) 150°, (c) 120°, and (d) 90° . . 78

Figure 7.20: Reconstructions of imaginary part of image with 15 views, when real and imaginary parts have similar physical boundaries, for different angular coverage of : (a) 180°, (b) 150°, (c) 120°, and (d) 90° 78

Part 1

Background

Chapter 1

Introduction

Science and technology has undergone a huge transformation over the span of the last century and half. More recently, the development of big computers have vastly accelerated the growth of new groundbreaking theories and also have served as a bridge between theory and experiments. Huge and highly complex problems which do not have closed form analytical solutions can now be easily solved using numerical techniques. Simulations can be used to predict outcomes from complex experiments eliminating the need for a large variety of time and labour intensive costly procedures. With the advent of computational techniques and capabilities, theory and experiment have merged almost seamlessly providing a great and exciting path towards scientific advancement and betterment of the human race. A great gift of modern science has been the domain of imaging sciences including a variety of imaging modalities. Simultaneously, the computational advancements have provided many robust schemes for image reconstruction from data acquired using these modalities. The applications have ranged across multiple disciplines: from x-ray crystallography to medical imaging, geophysical imaging to structural health monitoring and non-destructive evaluation of materials.

One of the most popular imaging techniques is tomography. The word tomography comes from the Greek word 'tomo' meaning a cut or section and 'graph' meaning a representation. So tomography involves getting cross sectional images of structures. In a very general sense, it is achieved by irradiating the object under test with some interrogating energy and then extracting the cross-sectional information from the resulting scattered energy from the object. Thus the scheme is a two-stage process. The first stage involves the data acquisition, where the object is irradiated and the scattered data collected. This data is generally referred to as the projection data. The second stage involves extracting the cross-sectional image by applying reconstruction algorithms to the projection data.

Based on the type of interrogating energy, tomography is broadly divided into two sub-categories. When the interrogating energy follows straight ray propagation, then it is called *Computed Tomography* or CT. The common examples are X-Ray CT, Single Photon Emission CT (SPECT), Positron emmission tomography (PET) etc. When the interrogating energy does not follow straight ray propagation, then it is called *Diffraction Tomography* or DT. Examples of DT are Magnetic Resonance Imaging (MRI), near field ultrasonic and microwave tomography. X-Ray is the most ubiquitous form of CT. So much so that CT by itself mostly conjures the idea of an X-ray CT system. It has come a long way since its first introduction by Hounsfield in 1970s as a commercially viable system. It has almost become a gold standard for fracture detection in medical as well as industrial applications. The high resolution of X-rays enable detection of minute defects (with 0.2 mm resolution) and anomalies in bones, metallic structures etc. The straight ray propagation also ensures simpler reconstruction algorithms as the diffraction effects are not considered.

In spite of its pervasiveness, X-ray has two major disadvantages. Firstly, the high energy of X-ray photons result in radiation damages in case of biological tissues. Further, while these are efficient in detecting structures of strong absorbers like bones and metal, X-rays are not as effective in differentiating between many types of soft tissue. Other CT scan techniques such as SPECT, PET etc also have a number of medical imaging applications.

In many real life scenarios, the interrogating energy that is used might not adhere to straight ray propagation. Depending on the sample being inspected, X-rays might not be the most effective form of interrogation. The optimum technique to use may be ultrasonics, microwaves or MR excitation. MRI is highly successful in soft tissue differentiation and is another gold-standard imaging scheme in medicine. Ultrasound has found applications in soft tissue imaging, bone imaging as well as in the NDT industry for defect detection in a variety of materials. These are examples of DT and hence the reconstruction algorithms need to take into account the diffracting nature of the incident waveform. Hence DT reconstruction algorithms have also been an active field of research. Conventionally, the projection data is gathered all around the specimen under test. However, generating a full 360° coverage has its own challenges. Depending on the application, generation of full 360° coverage might not be possible. It might be due to limited access around the specimen or the time required for full data acquisition might be too long in many scenarios. Further, for costlier imaging modalities like MRI, if the angular requirements can be lowered, then the overall cost of operation can also be reduced.

These issues have provided a significant impetus towards development of algorithms which can reconstruct images from limited angular coverage or incomplete projection data. This research explores algorithms for limited angle diffraction tomography. Broadly, two main aims are being explored. The first is using redundancies within the projection dataset to reconstruct complex valued images under moderately limited angular DT. The second is to apply various optimization and error minimization schemes for reconstruction from highly limited angular projection data.

The thesis is arranged as follows: in chapter 2, a brief background of diffraction tomography and the Filtered backpropagation (FBPP) technique for image reconstruction is given. In chapter 3, the data redundancy concept in DT projection data is introduced. Further, optimal ways to exploit this phenomenon in image reconstructions is discussed. Results from optimum reconstructions through exploiting redundancies are also presented in chapter 4. The last part of the thesis deals with application of a new technique for tomographic reconstruction Chapter 5 introduces the new area of research viz. *compressed sensing* (CS). Following a brief introduction on the subject, the framework for applying CS to image reconstruction from highly limited angular DT projection datasets is presented in chapter 6. Results from projection datasets from varying sparsity, both in terms of angular coverage and number of projections have been presented and analyzed chapter 7. Further, application of multiple sparse domains simultaneously has also been explored briefly. The importance of this is significant as higher data limitations than that allowed by regular CS might be achieved if multiple sparse domains are optimally exploited. The results show the effectiveness of CS as a stable algorithm to reconstruct complex valued images from severely limited DT projection data. Chapter 8 concludes the dissertation, summarizing the contributions of this work, its applications and possible future developments.

Chapter 2

Diffraction Tomography and Filtered Backpropagation technique

2.1 Introduction

Diffraction tomography (DT) is a popular imaging modality [2, 3], used in a variety of applications such as medical imaging, non-destructive evaluation of materials, structural health monitoring, geophysics e.g. [4–11]. In the domain of optical imaging this method has been explored in depth viz. optical diffraction tomography (ODT) with multi-disciplinary applications, see e.g. [12–18] etc. DT is a broad imaging technique of which ultrasound and microwave tomographic imaging are sub-classes. It is a comprehensive way of characterizing the complex permittivity or refactive index of the test sample. This is referred to as the object function. DT is applicable to microwave tomography of tissue samples and has been of great interest in tomographic imaging for breast cancer detection [19–22]. The high contrast of dielectric properties at microwave frequencies between healthy and cancerous breast tissue provides opportunities for clearly identifying malignancies within breast tissue. The contrast is much higher than in case of X-rays and hence microwave tomography is advantageous both in terms of true detection and avoiding radiation damage from X-rays. Further applications are in fields of SAR imaging. Various backprojection techniques have been explored for use in radar imaging and modified for better reconstructions [23–25]. Faster implementations for backprojections algorithms are also being explored e.g. [25]. Again, radar based methods have been combined with microwave tomography to generate higher resolutions for medical imaging [21]. Thus, any improvement in the traditional backpropagation techniques is of potential interest across multiple disciplines.

In the presence of weak scatterers, assuming the Born or Rytov approximations [3], the Fourier Diffraction Projection theorem (FDP) is applied. The FDP relates the scattered field data from the Region of Interest (ROI) to the 2D-Fourier Space of the ROI. Devaney developed the filtered backpropagation (FBPP) algorithm for this configuration to reconstruct a low-pass filtered image of the object function [2]. The traditional backpropagation technique requires projection data from $[0, 2\pi]$ angular coverage for accurate image reconstruction of a complex image. Even though the formulation applies to weak scatterers, it has found a number of applications and since its introduction, a steady research focus has been maintained to increase the extent of usage for backpropagation-like algorithms for DT and making them more general in applicability, e.g. [26, 27]. Some basic preliminaries leading to the FBPP algorithm are briefly introduced below. Some of the detailed derivations and explanations can be found in [3, 28, 29].

2.2 The Helmholtz Equation

The propagation of light or other electromagnetic wave through space or any medium obeys Maxwell's equations. Propagation through any homogeneous medium can be described through the wave equation, where the the vectorial description of the fields is simplified to a scalar description of waves. The general form of the wave equation is

$$\nabla^2 u(\mathbf{r},t) - \frac{1}{c^2}\frac{\partial^2}{\partial t^2}u(\mathbf{r},t) = 0. \tag{2.1}$$

This equation has both spatial and temporal variables. For analysis of time harmonic systems, we can only consider the time independent part, which gives us the standard general form of the wave equation:

$$\left[\nabla^2 + k^2(\mathbf{r})\right] u(\mathbf{r}) = 0. \tag{2.2}$$

where $k(\mathbf{r})$ is the wavenumber depending on the local permitivity or refractive index of the medium. If effects of polarization etc. are ignored, then $k(\mathbf{r})$ can be considered as a scalar depending on the refractive index $n(\mathbf{r})$ of the medium along with the variations $n_\delta(\mathbf{r})$:

$$k(\mathbf{r}) = k_0 n(\mathbf{r}) = k_0\left[1 + n_\delta(\mathbf{r})\right]. \tag{2.3}$$

In a homogeneous area, in absence of scatterers, the wave equation reduces to the homogeneous Helmholtz equation

$$\left[\nabla^2 + k^2\right] u(\mathbf{r}) = 0. \tag{2.4}$$

In the presence of an inhomogeneity or scatterer, n_δ represents the deviations in the refractive index within the object. So n_δ has bounded finite support within the object and is zero outside it. In this case, the form taken by the wave equation is called the inhomogeneous Helmholtz equation and is given by:

$$\left[\nabla^2 + k_0^2\right] u(\mathbf{r}) = -k_0^2 \left[n(\mathbf{r})^2 - 1\right] u(\mathbf{r}), \tag{2.5}$$

where $n(\mathbf{r})$ is the electromagnetic refractive index of the media given by:

$$n(\mathbf{r}) = \sqrt{\frac{\mu(\mathbf{r})\epsilon(\mathbf{r})}{\mu_0\epsilon_0}}, \tag{2.6}$$

where μ and ϵ are the permeability and dielectric constant variables. The right hand side of (2.5) is the forcing function of that equation. Let $o(\mathbf{r}) = k_0^2 \left[n(\mathbf{r})^2 - 1\right]$, so that the wave equation can be written as:

$$\left[\nabla^2 + k_0^2\right] u(\mathbf{r}) = -o(\mathbf{r})u(\mathbf{r}). \tag{2.7}$$

In order to deal with the inhomogeneity $o(\mathbf{r})$, the use of Green's function is applied [3]. The Green's function is the solution to:

$$\left[\nabla^2 + k_0^2\right] G(\mathbf{r} - \mathbf{r}') = -\delta(\mathbf{r} - \mathbf{r}'). \tag{2.8}$$

For the 2D case, it is a zero order Hankel function of first kind and takes the form:

$$G(\mathbf{r} - \mathbf{r}') = \frac{i}{4} H_0^{(1)}(k_0|\mathbf{r} - \mathbf{r}'\ |). \tag{2.9}$$

The object function of (2.8) can be considered as a point inhomogeneity. So the Green's function represents the field from a point scatterer. It is possible to represent the forcing function as an array of impulses, i.e.

$$o(\mathbf{r})u(\mathbf{r}) = \int o(\mathbf{r}')u(\mathbf{r}')\delta(\mathbf{r} - \mathbf{r}')d\mathbf{r}'. \tag{2.10}$$

Here, the forcing function of the inhomogeneous wave function is represented as summation of impulses weighted by $o(\mathbf{r})u(\mathbf{r})$ and shifted by $\mathbf{r} - \mathbf{r}'$. As the green's function represents the solution due to a single impulse function, and the left hand side of the wave equation is linear, therefore the total scattered field can be expressed as a summation of the scattered fields by each individual point scatterer. Using this idea, the total scattered field in the wave equation can be expressed as

$$u_s(\mathbf{r}) = \int o(\mathbf{r}')u(\mathbf{r}')G(\mathbf{r} - \mathbf{r}')d\mathbf{r}'. \tag{2.11}$$

Thus we arrive at an integral equation for the scattered field in terms of the total field, $u = u_0 + u_s$. The scattered field can be solved by applying some approximations. The two most popular approximations in this field are the *Born* approximation and the *Rytov* approximation. Both can be used to derive the *Fourier Diffraction Projection Theorem.* These approximations are briefly introduced below.

2.2.1 Born Approximation

The total field is the sum of the incident and the scattered field, i.e. $u(\mathbf{r}) = u_0(\mathbf{r}) + u_s(\mathbf{r})$. Using this in (2.11), have:

$$u_s(\mathbf{r}) = \int o(\mathbf{r}')u_0(\mathbf{r}')G(\mathbf{r}-\mathbf{r}')d\mathbf{r}' + \int o(\mathbf{r}')u_s(\mathbf{r}')G(\mathbf{r}-\mathbf{r}')d\mathbf{r}'. \tag{2.12}$$

In a Born approximation, the scattered field is assumed to be much smaller than the incident field. then, ignoring the second term of the right hand side of the equation above, it can be approximated as:

$$u_s(\mathbf{r}) \approx u_B(\mathbf{r}) = \int o(\mathbf{r}')u_0(\mathbf{r}')G(\mathbf{r}-\mathbf{r}')d\mathbf{r}'. \tag{2.13}$$

This is a first order approximation with respect to computing the scattered field. Higher order approximations can be applied by using the results of a Born approximated field to calculate the next order approximation. Effectively, the i^{th} order Born approximation field can be evaluated from the $(i-1)^{th}$ Born approximation result as:

$$u_B^{(i)}(\mathbf{r}) = \int o(\mathbf{r}')\left[u_0(\mathbf{r}') + u_B^{(i-1)}(\mathbf{r}')\right] G(\mathbf{r}-\mathbf{r}')d\mathbf{r}'. \tag{2.14}$$

As mentioned before, the first Born approximation is valid when the scattered field is smaller than the incident field. If the object is a homogeneous cylinder, then it becomes easy to evaluate the bounds of validity of the Born approximation. Let the radius be a and the change of refractive index within the cylinder be n_δ. Then for this cylinder, the total phase change a wave passing through it would undergo would be: $\triangle\phi = 4\pi n_\delta \, \frac{a}{\lambda}$, where λ is the wavelength of the incident wave. For the Born approximation to be valid, the necessary condition is that the total phase change should be should be less than π. Then the required bound becomes

$$an_{\delta} < \frac{\lambda}{4}. \tag{2.15}$$

2.2.2 Rytov Approximation

This approximation method applies a slightly different restriction. Here, the total field is represented through a complex phase: $u(\mathbf{r}) = e^{\phi(\mathbf{r})}$. Then the homogeneous wave equation can be rewritten as:

$$\begin{aligned} \left[\nabla^2 + k^2\right] u &= 0 \\ \text{or,} \quad \nabla^2 e^{\phi} + k^2 e^{\phi} &= 0 \\ \text{hence,} \quad \nabla^2 \phi + (\nabla\phi)^2 + k^2 &= 0 \\ \text{and finally with source,} \quad \nabla^2 \phi + (\nabla\phi)^2 + k_0^2 &= -o(\mathbf{r}). \end{aligned}$$

All the fields ϕ have their spatial argument $\mathbf{r}$ dropped for ntoational convenience. Starting here and assuming that $\phi = \phi_0 + \phi_s$, where, $u_0 = e^{\phi_0(\mathbf{r})}$ and proceeding similsrly to the Born approx. scenario, the necessary condition for the Rytov condition to hold is shown to be:

$$n_{\delta} > \left[\frac{\nabla\phi_s\lambda}{2\pi}\right]^2. \tag{2.16}$$

This connects the change in the refractive index with the gradient of phase. A more practical form can be derived:

$$|\nabla n(\mathbf{r})| < \frac{\sqrt{2n_0|n(\mathbf{r}) - n_0|}}{\lambda}, \tag{2.17}$$

where, n_0 is the refractive index of the background medium. This equation presents a validity condition which is dependent on the gradient of refractive index change within the sample rather than the absolute value or thickness of the sample. This makes the Rytov approximation applicable to biological samples.

2.3 Fourier Diffraction Projection Theorem (FDPT)

The fundamental theory underlying 2D-DT is the FDPT which relates the scattered field data from the Region of Interest (ROI) due to incident plane waves to the 2D-Fourier space of the ROI [3]. It employs conditions of weak scattering i.e. the Born or Rytov approximations. The traditional 2D-configuration is shown in Fig. 2.1. If the object $o(x, y)$ is illuminated with a monochromatic plane wave of frequency ν_0 incident at an angle ϕ to the horizontal axis, the 1D Fourier Transform (FT) of the scattered field measured along the straight line $\eta = l$ in the co-ordinate system (ξ, η) gives the values of the 2D transform of the object $O(\nu_x, \nu_y)$ along a semi-circular arc AOB in the frequency domain, at angle ϕ as shown in the right half of Fig. 2.1. The scattered field data and the object function are related by the following equation:

$$U(\nu, l) = \frac{j}{2\sqrt{\nu_0^2 - \nu^2}} e^{j\sqrt{\nu_0^2-\nu^2}l} O\left(\nu, \sqrt{\nu_0^2 - \nu^2} - \nu_0\right), \tag{2.18}$$

where $U(\nu, l)$ represents 1D FT of the scattered field, $u(\xi, \eta)$ under Born approximation (measured at line $\eta = l$), and ν lies in the range $[-\nu_0, \nu_0]$.

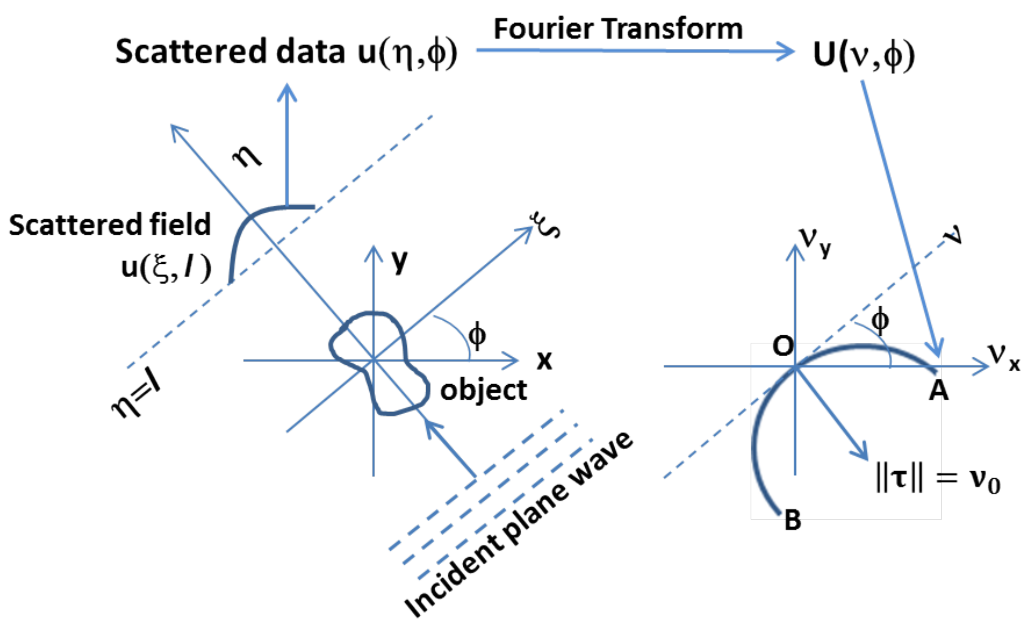

Figure 2.1: Classical scan configuration of 2D DT (left) and relation of scattered field data with the 2D Fourier space of the objective function (right).

2.4 Filtered Backpropagation Algorithm

Starting with the Fourier Diffraction Projection theorem, Devaney developed the well-known filtered backpropagation method in [2]. In polar coordinates, as presented in [30], the backpropagation integral takes the form:

$$a(r,\theta) = \int_{\phi=0}^{2\pi} \int_{\nu_m=-\nu_0}^{\nu_0} \frac{\nu_0}{\nu'} |\nu_m| \, M(\nu_m, \phi) e^{[j2\pi\nu_m \cos(\phi-\alpha-\theta)]} d\nu_m d\phi. \tag{2.19}$$

In (2.19), $a(r,\theta)$ is the object function being reconstructed in polar spatial coordinates (r,θ), ν_0 is the frequency of the incident monochromatic plane wave and ϕ being the incidence angle, $M(\nu_m, \phi)$ is a modified 1D FT of the scattered data, defined as

$$M(\nu_m, \phi) = U(\nu_m, \phi) \frac{j\nu'}{2\pi^2 \nu_0^2} e^{-j2\pi\nu' l}, \tag{2.20}$$

where $\quad \nu' = \sqrt{\nu_0^2 - \nu_m^2}, \qquad \nu_a = \mathrm{sgn}(\nu_m)\sqrt{\nu_m^2 - \nu_\mu^2}, \qquad \nu_\mu = j(\nu' - \nu_0)$ and

$$\alpha = \mathrm{sgn}(\nu_m) \arcsin\left(\frac{1}{2\nu_0}\sqrt{\nu_m^2 - \nu_\mu^2}\right), \tag{2.21}$$

and also, α could be further simplified to

$$\alpha = \frac{1}{2} \arcsin\left(\frac{\nu_m}{\nu_0}\right). \tag{2.22}$$

In order to reconstruct a complex object accurately, a full knowledge of $M(\nu_m, \phi)$ in the range $[0, 2\pi]$ is necessary to perform the integration in (2.19), [31]. Using the projection data from a full 360° coverage, the filtered backpropagation integral reconstructs a low-pass filtered version of a complex-valued object function. The next part of the thesis presents the inherent redundancies in a full projection dataset in DT and demonstrates efficient ways to exploit that.

Part 2

Accurate Reconstruction From Moderately Limited Projection Data

Chapter 3

Data Redundancy in Diffraction Tomography

A major challenge in many real world situations is that projection measurements cannot be gathered over full 360° view around the test object. With limited access to the object and decrease in angular coverage, the available data in the Fourier space decreases. Reconstruction from this partial Fourier space data leads to many artifacts and loss of important image features. Hence alternate schemes are needed for image reconstruction from limited angular coverage projection data. For highly sparse data or limited angular access various minimization, regularization, estimation techniques and statistical approaches are being successfully explored to make the reconstruction algorithms more robust to sparse and noisy data e.g. [32–34]. However, generally these are iterative methods and the total computation time depends on the convergence rate of the algorithm. A single step method would always be fast and desirable provided it can handle the limited availability of data.

In [30, 35, 36], a novel alternative approach for moderately limited angular access was introduced. It was shown that using inherent redundancies in the projection data from the conventional setup, exact reconstruction is possible with data from $[0, 3\pi/2]$ coverage. This redundancy and the reconstruction method from lower coverage utilizing this is explained next.

Consider the two arcs OA and OB in Fig. 2.1 from the semi circle AOB. The two arcs individually traverse the transform space (i.e. the Fourier space) as the projection angle changes between $[0, 2\pi]$. Now consider their traversals in the Fourier space individually for angular coverage of $[0, 3\pi/2]$. This is illustrated in Fig. 3.1 below. Individually each half does an incomplete traversal of the Fourier space as shown in Fig. 3.1(a) and 3.1(b). However, if superimposed, as seen in Fig. 3.1(c), the entire Fourier space is covered with some areas of overlap. The key point is that at 270° there is in effect, a complete coverage of the Fourier space. This scan range of $[0, 270°]$ is referred to as the minimal scan angle and is the minimal angular coverage required for exact reconstruction [30].

To better appreciate the principle, the Fourier space domain is re-plotted in a modified coordinate system, where the spatial frequency is plotted along x-axis and the angular coverage along y-axis. Physically, it can be viewed as straightening out the arcs AOB for different projection angles and stacking them up on top of each other sequentially. In this layout, the entire Fourier dataspace can be divided into four sub-regions A, B, C and D as shown in Fig. 3.1(d) where the boundaries for the four regions can be expressed as $A = [|\nu_m| \leq \nu_0, 0 \leq \phi < 2\alpha + \pi/2]$, $B = [|\nu_m| \leq \nu_0, \pi/2 + 2\alpha \leq \phi < 2\alpha + \pi]$, $C = [|\nu_m| \leq \nu_0, \pi + 2\alpha \leq \phi < 3\pi/2]$ and $D = [|\nu_m| \leq \nu_0, 3\pi/2 \leq \phi < 2\pi]$. As seen in (2.22), α is a function of ν_m and so the regions have nonlinear boundaries.

From FDP theorem the following periodicity holds [37]:

$$M(\nu_m, \phi) = M(-\nu_m, \phi + \pi - 2\alpha), \tag{3.1}$$

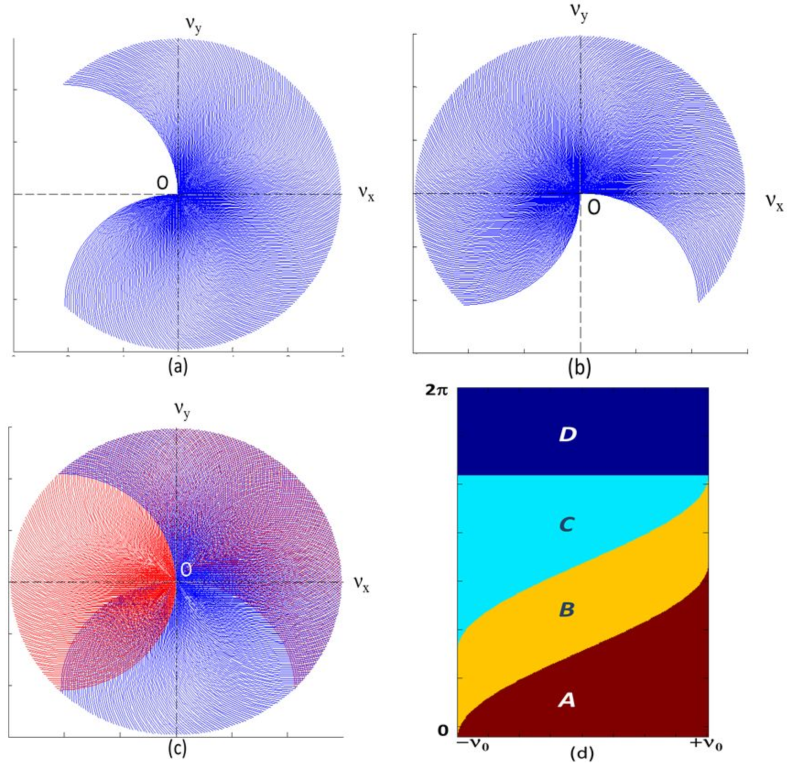

Figure 3.1: (a) Fourier space coverage for 270° angular access by segment OB in fig.1 (b) same for segment OA of fig-1. (c) Superposition of the two coverages from (a) and (b). (d) The Fourier data-space in alternate co-ordinate system with angular coverage along y-axis and the frequency along x-axis.

which also implies that for every point in region A (or B), there is a point having equal value for the Fourier coefficient in region C (or D). Thus, the knowledge of $M(\nu_m, \phi)$ in regions A and B, makes information in C and D redundant. This redundancy can be handled by normalizing the dataspace using appropriate weight filters. The weighted dataset $M'(\nu_m, \phi)$ can be defined as $M'(\nu_m, \phi) = w(\nu_m, \phi) M(\nu_m, \phi)$, where $w(\nu_m, \phi)$ satisfies the condition

$$w(\nu_m, \phi) + w(-\nu_m, \phi + \pi - 2\alpha) = 1. \tag{3.2}$$

It should be noted that since region D is unavailable in a 270° coverage we set $w(\nu_m, \phi) = 0$ in region D and correspondingly $w(\nu_m, \phi) = 1$ in region B. For regions A and C, any weight function is valid as long as it satisfies (3.2). Using the weighted dataset $M'(\nu_m, \phi)$ we can apply the regular backpropagation algorithm for reconstruction. This is called Minimal-Scan Filtered Backpropagation (MS-FBPP) which involves evaluating the following integral

$$a^W(r, \theta) = \frac{1}{2} \int_{\phi=0}^{3\pi/2} \int_{\nu_m=-\nu_0}^{\nu_0} \frac{\nu_0}{\nu'} |\nu_m| M'(\nu_m, \phi) e^{[j2\pi\nu_m \cos(\phi-\alpha-\theta)]} d\nu_m d\phi. \tag{3.3}$$

This integral can in theory exactly reconstruct an image from a 270° angular coverage by utilizing data redundancy in projection data. The weights $w(\nu_m, \phi)$ can then be used to define classes of backpropagation algorithms for image reconstruction. An example of weight functions introduced in [30] is given in equation below:

$$w(\nu_m, \phi) = \begin{cases} \sin^2\left[\frac{\pi}{4} \frac{\phi}{\pi/4+\alpha}\right], & \text{in } A, \\ 1, & \text{in } B, \\ \sin^2\left[\frac{\pi}{4} \frac{3\pi/2-\phi}{\pi/4-\alpha}\right], & \text{in } C, \\ 0, & \text{in } D. \end{cases} \tag{3.4}$$

This will be used as a reference later on in Section 4 for comparison with the weight functions that are proposed in this thesis. The filter of (3.4) will be referred to as the sine-squared filter hereon. This is a very elegant and simple filter designed to have continuity across the boundaries between regions A, B, C and D. To demonstrate the efficacy of

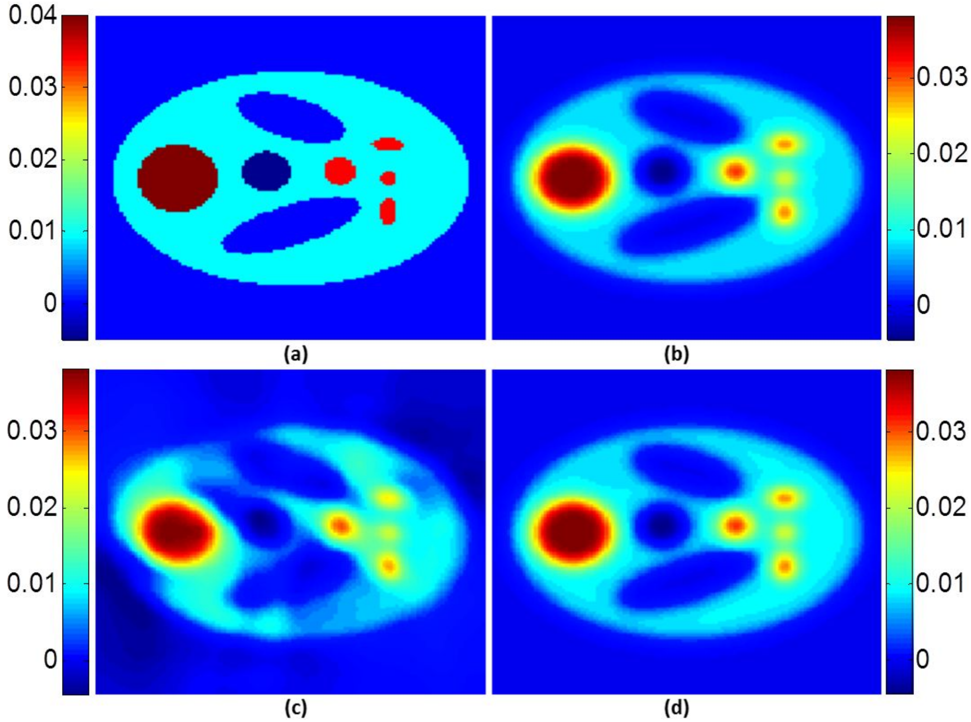

Figure 3.2: Demonstration of the MS-FBPP concept (a) real part of original image, (b) FBPP reconstruction from 360° coverage (c) FBPP reconstruction from 270° coverage and (d) MS-FBPP reconstruction from 270° coverage

MS-FBPP, a sample reconstruction is performed on a Shepp-Logan type phantom with complex parameter distribution. The real part of the phantom is shown in Fig. 3.2(a) and the imaginary part in Fig. 3.3(a). Reconstruction from regular FBPP and MS-FBPP using weights of (3.4) are given in Fig. 3.2 and Fig. 3.3. The images show the MS-FBPP algorithms capable of generating accurate reconstructions from 270° (equivalent to full coverage), whereas the regular FBPP image shows considerable distortion at 270°.

Weight filters which are discontinuous across boundaries of the four regions in Fig. 3.1(d) can give rise to artifacts, especially in case of discrete data. Further, for each class of weights, its distribution in frequency space of Fig. 3.1(d) also determines the performance when the available coverage is below 270°. This is because, C and D are

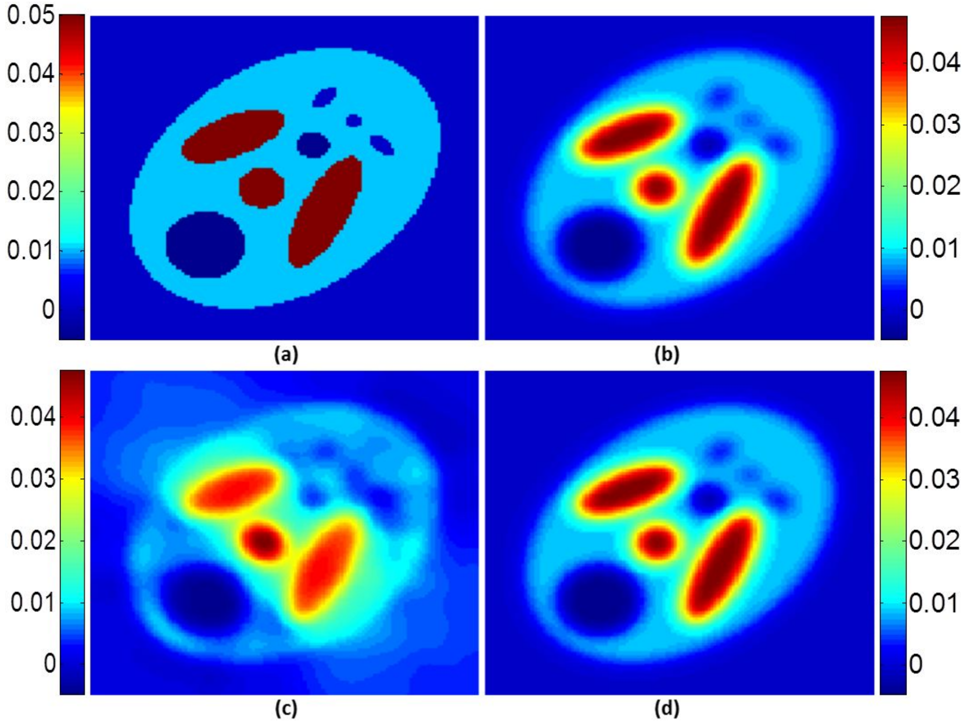

Figure 3.3: Demonstration of the MS-FBPP concept (a) imaginary part of original image, (b) FBPP reconstruction from 360° coverage (c) FBPP reconstruction from 270° coverage and (d) MS-FBPP reconstruction from 270° coverage

complementary to regions A and B respectively. An efficient weight function set would be that which spans most of the regions A and B, thus limiting the requirement to access regions C and D. In effect such weights can generate good reconstructions even when the angular coverage is less than 270°. The next section explains a systematic approach to generate general classes of weight functions.

3.1 Generation of Efficient Weight Functions

For lower angular coverages, the algorithm using sine-squared weights results in significant distortions. In this section a technique is explored that efficiently uses the redundancies in the Fourier space data using the conventional setup [38]. This technique can reconstruct better images (than regular FBPP) effectively over any range between π to $3\pi/2$. This is a crucial development, as the demands on angular access for complex valued object reconstruction is lowered considerably. The projection datasets are used optimally to get enhanced reconstructions from lower angular coverages. Also, this is a direct reconstruction method which does not employ any error minimization algorithms and hence is faster and accurate over angular coverages between 180°-270°. From previous section, we see that the weights in regions B and D are 1 and 0 respectively. Notice that weights in region C can be generated from weights of region A, because for any point (ν_m, ϕ) in region C, the point $(-\nu_m, \phi + \pi - 2\alpha)$ in A is equivalent due to (3.1), and we get $w(\nu_m, \phi) = 1 - w(-\nu_m, \phi + \pi - 2\alpha)$, using (3.2). Thus it is sufficient to generate weights for the region A only.

Furthermore from (3.2), the non-negative weights are bounded above by 1. So in region A, for any fixed ν_m, the function $w(\nu_m, \cdot) =: F(\cdot)$ is defined on $[0, 2\alpha + \pi/2]$, and takes values between 0 and 1. However it is desirable to have weights which are continuous at the boundaries between two regions. Weights which are discontinuous at the boundaries will generate artifacts in case of discrete datasets as noticed in [30].

Here we propose an approach to generate the weights, by using cumulative distribution functions (cdf) to model $F(\cdot)$, which are guaranteed to be bounded within 0 and 1. To obtain continuous weights, we use continuous F with

$$F(0) = 0, \quad \text{and} \quad F(2\alpha + \pi/2) = 1. \tag{3.5}$$

This will ensure that weights are continuous at the boundary between regions A and

B, and consequently at the boundaries between regions B and C, and C and D. This approach would allow us to choose weights from a number of cdfs. In this dissertation, we primarily use beta-cdf to generate weights. The standard beta-cdf is defined as:

$$F(x|a,b) = \int_{-\infty}^{x} f(t|a,b)dt. \tag{3.6}$$

Where $a > 0$, $b > 0$, and f is the standard beta probability density function:

$$f(t|a,b) = \begin{cases} \frac{1}{B(a,b)} t^{a-1}(1-t)^{b-1}, & 0 \leq t \leq 1, \\ 0, & \text{otherwise}, \end{cases} \tag{3.7}$$

and $B(a,b) = \int_0^1 t^{a-1}(1-t)^{b-1}dt$. We obtain family of beta-cdf's by changing values of a and b in (3.7), as shown in Fig. 3.4. Notice that, the standard beta-cdf has support $[0,1]$, while in region A for a fixed ν_m, we need to define weights for $\phi \in [0, 2\alpha + \pi/2]$. This can be achieved by substituting $x = \frac{\phi}{2\alpha+\pi/2}$ in (3.6). The corresponding weight profiles in the frequency domain are shown in Fig. 3.5.

The plots in Fig. 3.4 can be used to understand how the weights will be distributed in Regions A and C. Fig. 3.5 gives useful insight on choosing optimal parameter values. For example, with combinations $a = 2, b = 5$ or $a = 6, b = 1$, region A is not well covered, whereas for $a = 0.4, b = 6$, region A has been almost fully covered with near unity weights leaving Region C with mostly near-zero weights. This combination is expected to better utilize data redundancy than the other combinations shown in Fig. 3.4.

This can be further illustrated through Fig. 3.6 and Fig. 3.7. Fig. 3.6 shows some weight distributions in the Fourier space (in the modified co-ordinate system).The beta-

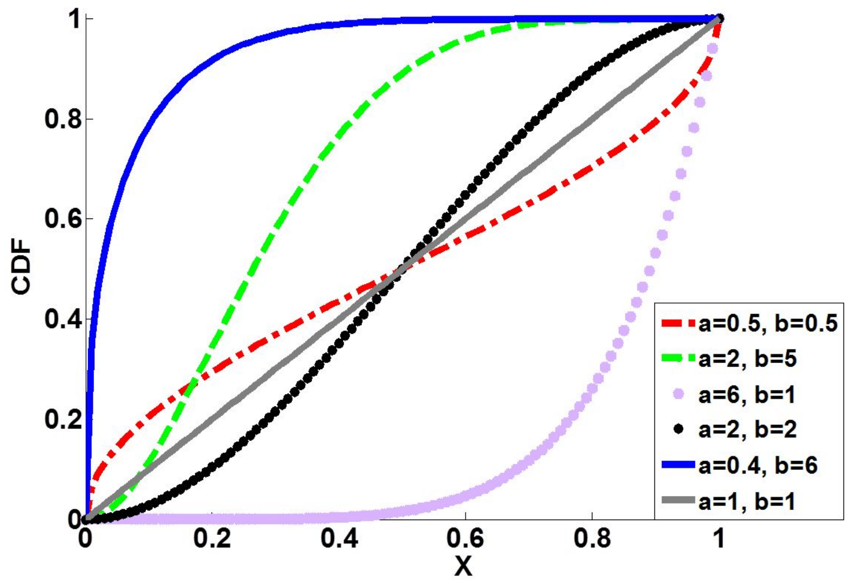

Figure 3.4: Beta-cdf plots for different values of the parameters a and b

cdf parameters used to generate these weights are shown in inset white text. Fig. 3.7 shows the reconstructed real parts of the images by using these weights. The weights which cover region A more completely also give better reconstructions.

It should be noted that especially for coverages less than 270°, we receive less information from C, hence an optimum weight function should span most of region A with near unit weight. Since the weights are continuous across the boundaries of the regions, the lower boundary of A (with region D) starts from zero and ends with unity at the boundary with B. The transition from zero to unity should be adequate to retain as much information as possible within region A. Then the loss of information in region C would not affect the reconstruction quality. In this thesis, we demonstrate the efficacy of using cdf based weights in image reconstruction at sub-minimal angular coverage. To do this, optimum values of parameters were heuristically determined in the following manner: for the beta-cdf, a parametric sweep over the range of $a \in [0.2, 3]$, $b \in [1, 6]$ was performed and

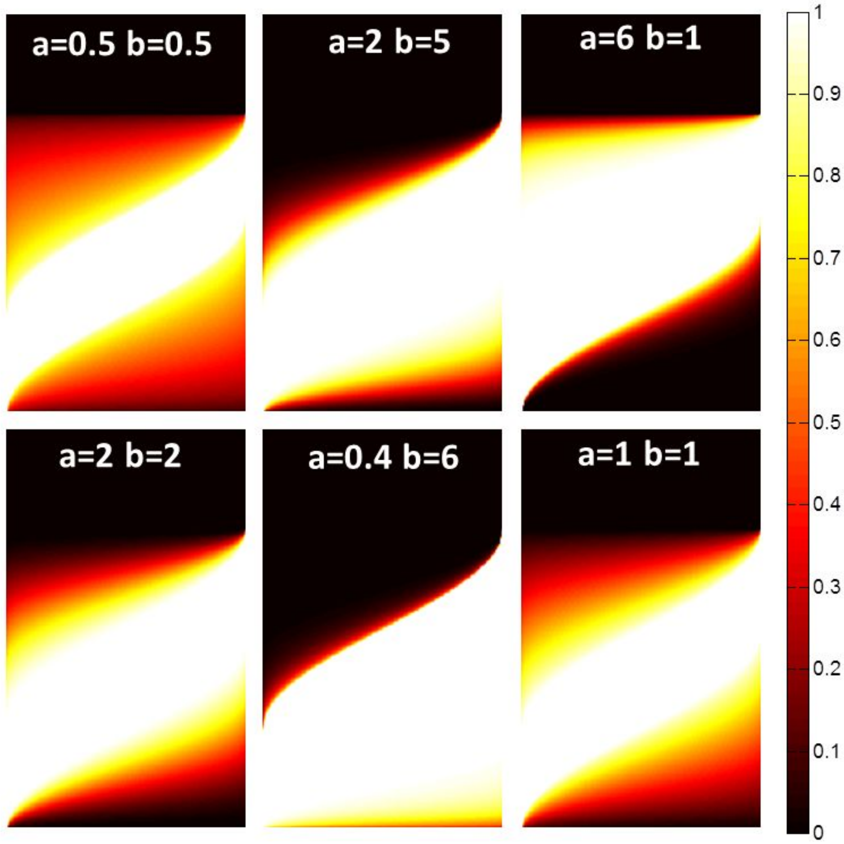

Figure 3.5: Images showing weight distributions in Fourier domain generated by parametric variation of the beta-cdf (using the parameters shown in Fig. 3.4). Frequency is plotted along abscissa and angular coverage along ordinate.

the corresponding weight distributions were generated. Reconstructions were performed with these weights for a sub-minimal coverage of 200°. The weight combination which gave the least distortion in the reconstruction and maintained highest correlation with the original image was chosen as the optimum set. Within this range, the combination $a = 0.4$, $b = 6$ gave best results and is used for image reconstruction in the next section.

Similar approach can be used to generate weight functions from other cumulative distribution functions as well, for instance with the gamma-cdf. However, since the gamma distribution has unbounded support, a suitable transformation of the argument is required to ensure that the weights are constructed with continuity properties at the boundaries

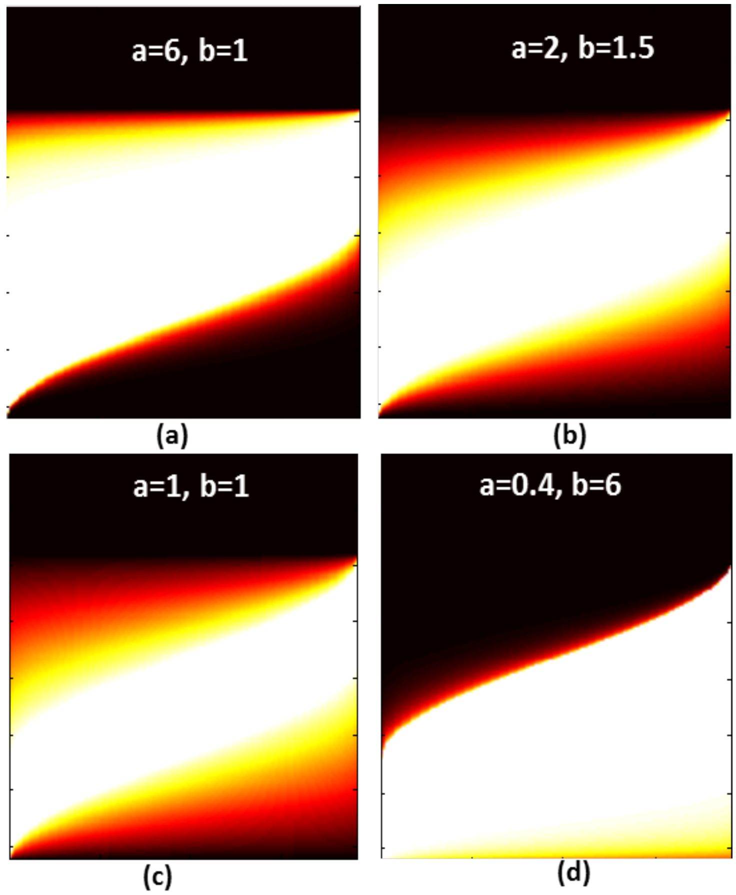

Figure 3.6: Images showing weight distributions in Fourier domain generated by parametric variation of the beta-cdf. The parameters a and b used for each weight distribution are inset in each plot. Frequency is plotted along abscissa and angular coverage along ordinate.

as discussed above. Details about constructing the weights with gamma-cdf are described in appendix-A. For this case, the parameters were varied in the range $a \in [0.1, 3.1]$, $b \in [0.1, 3.1]$. The best parameter set found from this range was $a = 2.1$, $b = 0.1$. In the following chapter, results from beta and gamma distributions using these optimum parameters for each distribution will be presented and compared with the results from using weights given in (3.4). Their performance under the presence of noise will also be evaluated.

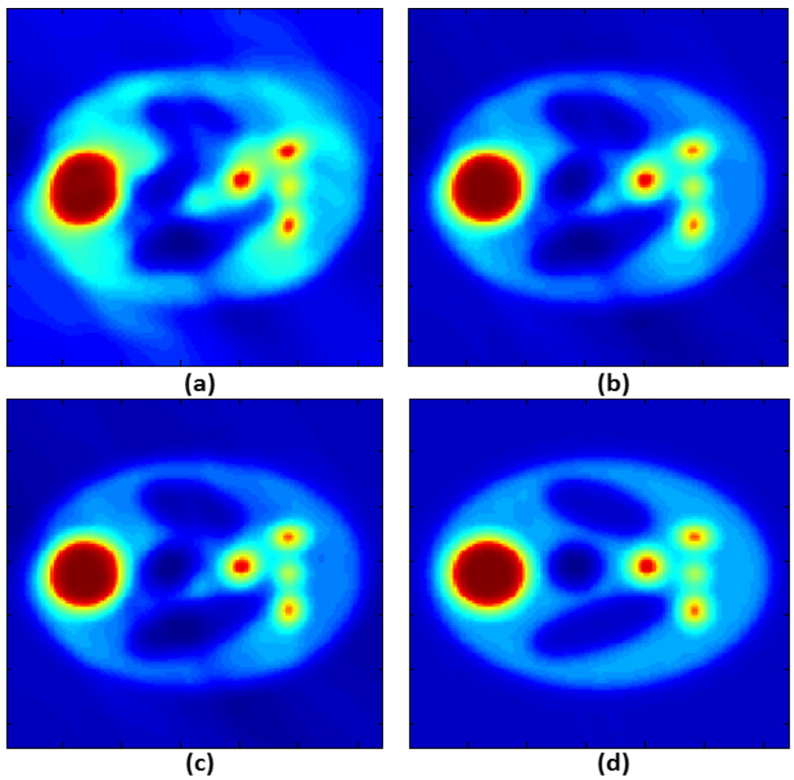

Figure 3.7: Corresponding reconstructions from using the weight distributions in Fig. 3.6

Chapter 4

Accurate Reconstructions for Moderately Limited Angular Measurements

In this chapter results from simulated projection data for DT are presented.The test image is complex. Both the real and imaginary parts of the image are in effect, modified versions of the Shepp-Logan phantom, a standard model used to validate computed tomography algorithms. The real and imaginary parts of the test image are shown in Fig. 3.2(a) and 3.3(a). The projection data from the phantom was computed following [30,37]. The image matrix is 128×128 pixels with pixel size of $\lambda/8$. The image has an area of $16\lambda \times 16\lambda$. The objective of this section of the thesis was to define a procedure to generate optimum weights which can exploit the redundancy for angular coverages below $270°$ and up to $180°$, where redundancy is still present in the projection data.

4.1 Noiseless Reconstruction

Proceeding in the manner described in the previous section to generate weights, the following optimum parameters for different cdfs were used: for beta-cdf, $a = 0.4, b = 6$;

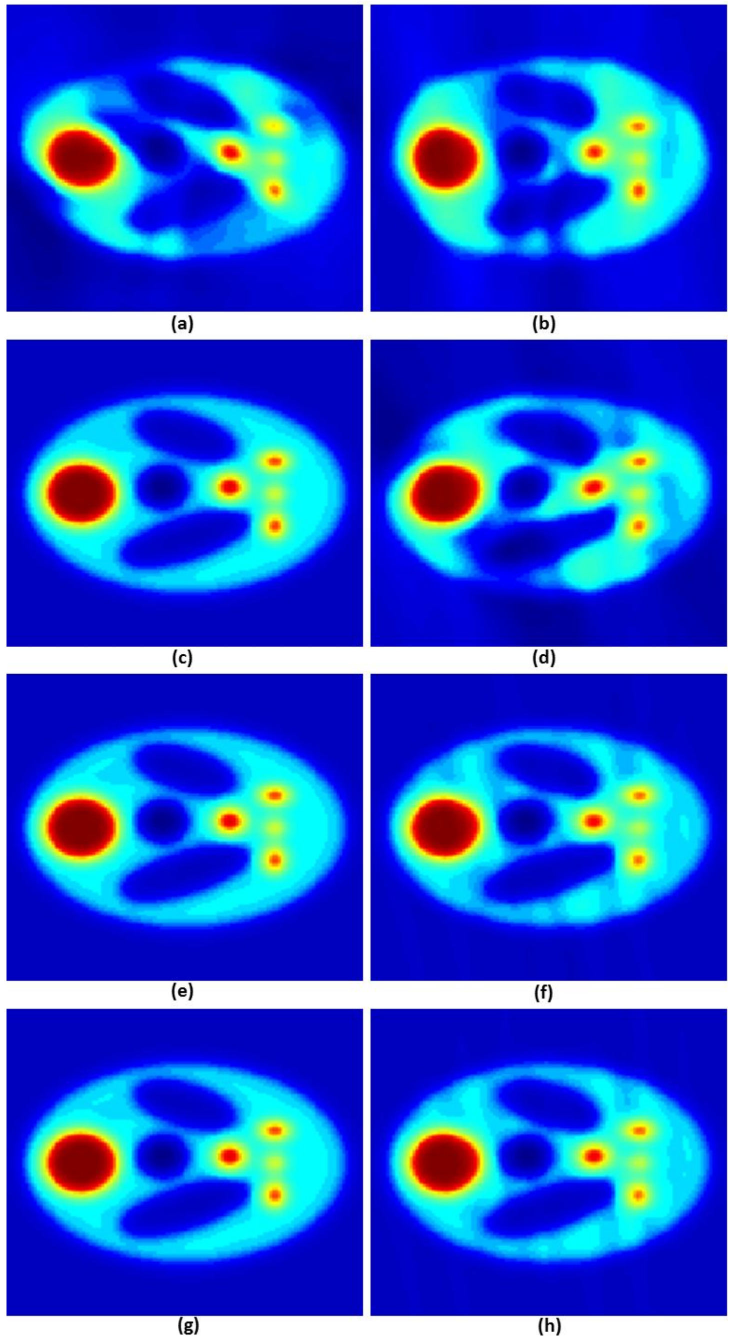

Figure 4.1: Reconstructed real part from complex test image under noiseless conditions. The left column shows reconstruction from 270° coverage and right column shows reconstruction from 200° coverage. (a)-(b) using regular FBPP, (c)-(d) using sine-sq weights, (e)-(f) using gamma-cdf weights, (g)-(h) using beta-cdf weights

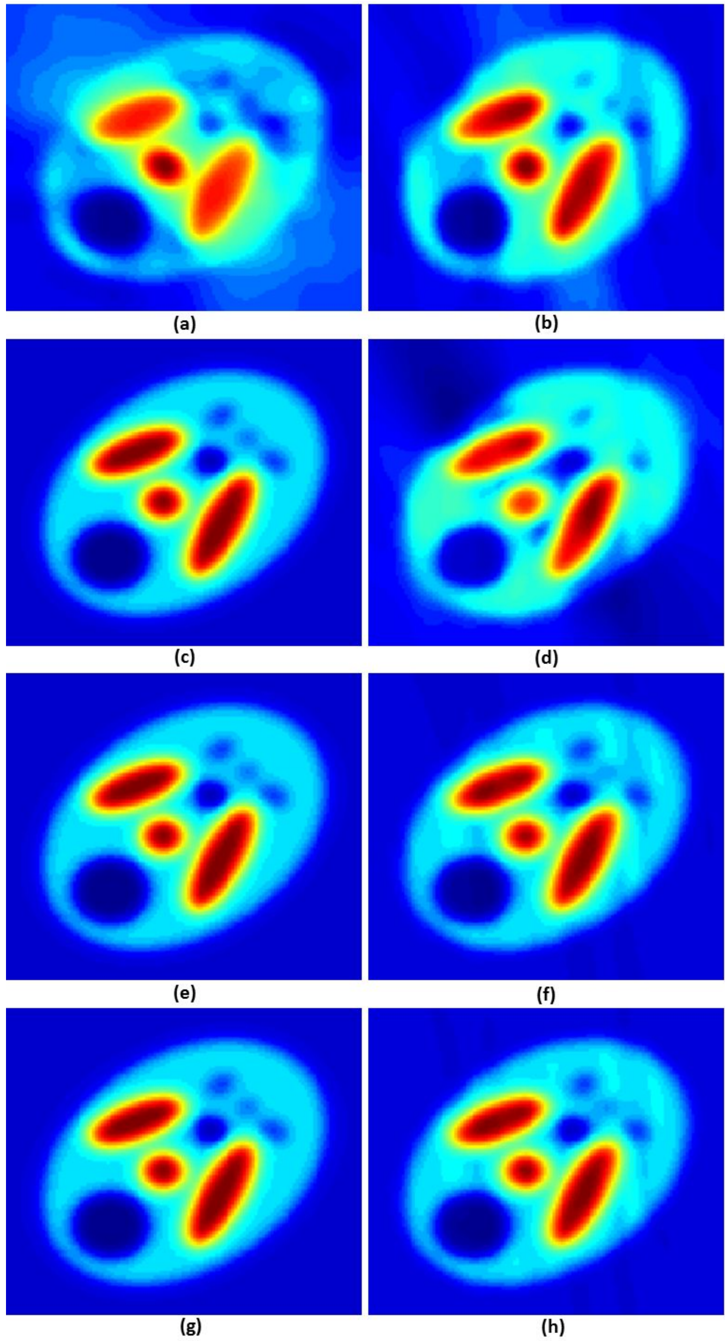

Figure 4.2: Reconstructed imaginary part from complex test image under noiseless conditions. The left column shows reconstruction from 270° coverage and right column shows reconstruction from 200° coverage. (a)-(b) using regular FBPP, (c)-(d) using sine-sq weights, (e)-(f) using gamma-cdf weights, (g)-(h) using beta-cdf weights

for gamma-cdf, $a = 2.1, b = 0.1$. Reconstructed images have been plotted from regular FBPP and MS-FBPP using different weight functions for coverages 270° and 200° (an example of sub-minimal angular coverage). Both real and imaginary parts are shown in Fig. 4.1 and 4.2 respectively. The reconstructions show the beta-cdf and gamma-cdf based weights generate a very stable reconstruction even in lower angular coverage of 200°, with beta-cdf performing slightly better overall.

To compare the performance of the different MS-FBPP algorithms quantitatively, we use their Mean-Absolute-Error (MAE) with respect to the original image. The MAE is calculated as the absolute mean pixel-by-pixel difference between the original and reconstructed image: $MAE = \frac{1}{n} \sum |im_{or}(i) - im_{re}(i)|$, where $im_{or}(i)$ is the intensity of the i^{th} pixel in the original image and $im_{re}(i)$, the intensity of the i^{th} pixel in the reconstructed image and n is the total number of pixels in the image. The errors in real and imaginary parts of image were calculated separately. At 200° coverage, for the real part of the image, the beta-cdf based reconstruction had a 30.77% lower error than regular FBPP, while the gamma-cdf based reconstruction yielded a 29.11% lower error. A similar trend is seen for the imaginary part of the image. The sine-squared based weights give accurate reconstructions at 270°, but below 270° they progressively deteriorate. These are clearly not optimum choices for coverage $< 270°$. For example, at 200° coverage, the quality of reconstruction degrades for both the regular FBPP and sine-squared weighted FBPP. However, the latter has a higher error than the regular FBPP reconstruction (2.46% higher in real part of image). A more detailed error-analysis has been done with noisy data in the next subsection. Below 180° coverage, the redundancy disappears and using weights alone, in principle cannot produce a better reconstruction than regular FBPP. So, reconstructed images are not shown for further lower coverage. However, it should be noted that for such lower coverage, reconstruction from un-optimized weights will generate higher errors than regular FBPP. This is also evident from the sine-square weighted reconstructions for sub-minimal coverage.

4.2 Reconstruction with Noisy Data

Noise is an integral part of any measurement system. In a DT setup, noise may arise from random inhomogeneities in medium or may be introduced by the experimental procedure. To account for these, noisy reconstruction has been modeled as a stochastic process in literature [39], [40]. Reconstruction from noisy data is necessary to examine the reliability of these algorithms when applied to practical systems. The MS-FBPP algorithms are expected to respond to noisy data models differently. To consider the effect of all noise sources, it was assumed as sufficient to consider a white Gaussian noise distribution in the scattered field data [37]. An additive white Gaussian noise (AWGN) with different variances has been injected to the analytically computed projection data to give different noise levels. To observe the effect of noise, we compared the reconstruction from the weighted MS-FBPP algorithms with regular FBPP using the projection data injected with 3-dB AWGN. The reconstructed images from noisy data using beta-cdf weights for different angular coverages in the range of $[200^\circ,\ 270^\circ]$ are given in Fig. 4.3 and Fig. 4.4. We use here weights based on beta-cdf with $a = 0.4$, $b = 6$, which earlier gave best results with noiseless data. The reconstructions show robustness of the algorithm to noise levels that can be considered to be reasonable in good experimental data.

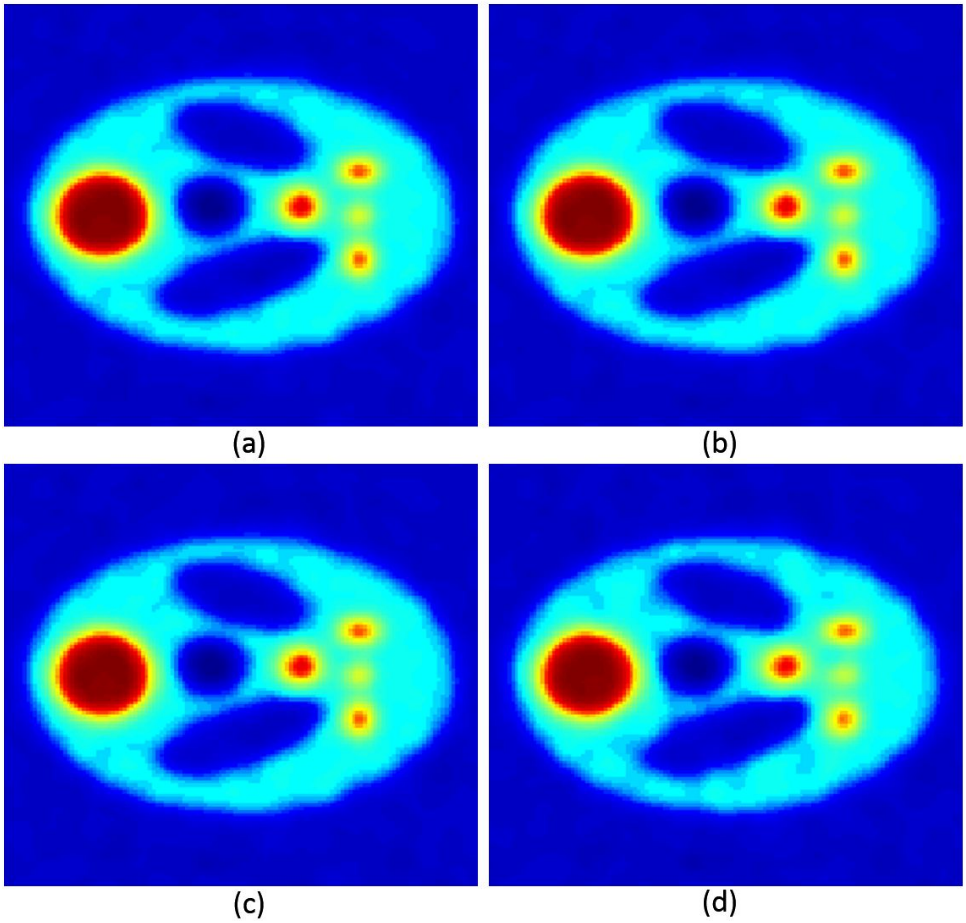

Figure 4.3: Reconstruction of real part of image from 3dB awgn projection data using beta-cdf weights for angular coverages (a) 270° (b) 250° (c) 220° (d) 200°

Fig. 4.3 and Fig. 4.4 show that the beta-cdf based weights are capable of maintaining all the features and without significant distortions up to 220° with 43.1% improvement of MAE over regular FBPP in real part and 38.7% in imaginary part of the image. The reconstruction at 200° is also almost distortionless with the error improvement figures being 27.8% and 19.4% for the real and imaginary parts respectively. The responses are stable and the images are not affected noticeably due to the noise injection as seen in these figures. A detailed discussion of the performance in terms of MAE is given next.

The MAE calculated for the different weights at different angular coverages are plotted

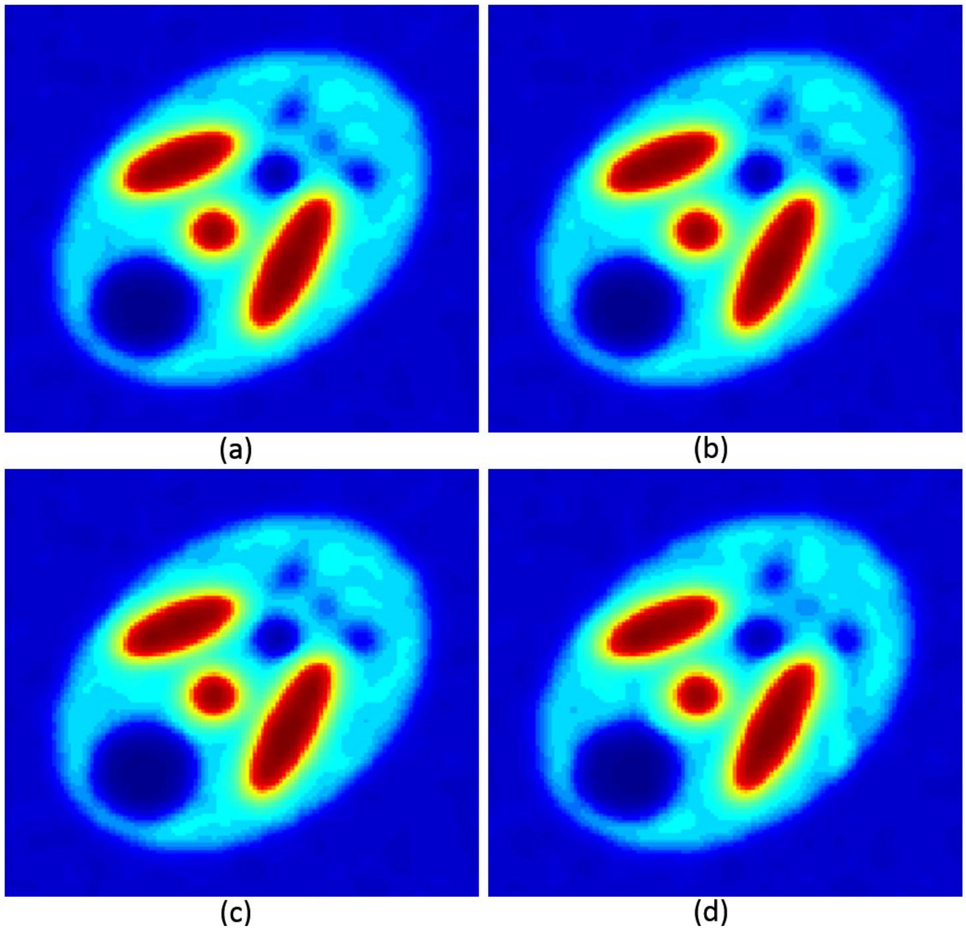

Figure 4.4: Reconstruction of imaginary part of image from 3dB awgn projection data using beta-cdf weights for angular coverages (a) 270° (b) 250° (c) 220° (d) 200°

in Fig. 4.5 and Fig. 4.6. The plots show that as the coverage goes further below 270°, the beta-cdf and gamma-cdf weights are able to generate MAEs which remain lower than regular FBPP and are very steady up to 200°. For the beta-cdf based reconstruction, as the coverage decreases from 270° to 200°, the value of MAE increases by only 2.33% in the real part and 1.45% in the imaginary part. For gamma-cdf based reconstruction, the numbers are 4.31% and 2.64% respectively. For coverages below 200°, as the redundancy is lost, these two MAEs increase and slowly converge towards the MAE of a regular FBPP reconstruction around 180°. For the sine-squared based weights, the MAEs are almost equal to the other two weights (beta and gamma cdf) in the interval $[250°, 270°]$, but rapidly increases as the coverage reduces, and become greater than the regular FBPP and other two cdf weighted reconstructions. At 200° coverage, the MAE of the real part of the image increases by as much as 46.05% of its value at 270° coverage and that of the imaginary part by 48.62%.

The MAE plots for the regular FBPP algorithm in Fig. 4.5 and Fig. 4.6 may look counterintuitive. This is because the error increases as the angular coverage increases from 180° to 270°. However, it should be noted that starting from 180° coverage and above, there are regions in the Fourier space where there is overlap from the two halves OA and OB of the semi-circular arc AOB in Fig. 2.1. The regular FBPP doesn't apply weights to the dataspace to account for these partial overlaps and hence gives higher errors in reconstruction. At 360° coverage, as there is complete coverage by both the arcs OA and OB, weighting the dataspace is not required. Following this, it is found that error increases from 180° coverage to a maximum at 270°, where there is maximum asymmetry with respect to overlapping coverage in Fourier space by the two half semi-circles, OA and OB. Weighting becomes most important at 270°. Beyond that, the importance decreases again and vanishes at 360° coverage. For this reason, an error increase is seen between 180° and 270° coverage. The solution to this problem in that coverage range is to normalize the projection data with optimal weights before applying the backpropagation algorithm.

The percentage improvements of MAE for all the three filter classes with respect to the regular FBPP are plotted in Fig. 4.7 and Fig. 4.8. All the weights show maximum improvement at 270°, and it decreases as the coverage gets more limited. The degradation of sine-squared filters is much greater than the cdf based filters. The plots show that at

180°, with the disappearance of redundancy within the projection data, the MAEs for regular FBPP and that of beta-weighted MS-FBPP converge. In contrast, for the sine-squared weights, the MAE steadily increases and becomes greater than the MAE from regular FBPP. This is expected and demonstrates the effectiveness of the beta-cdf based weights as an optimal choice. The gamma-cdf based reconstruction behaves similarly with a slightly higher MAE (1.66% higher than beta-cdf reconstruction in real part of image and 1.32% higher for the imaginary part of the image at 200° coverage).

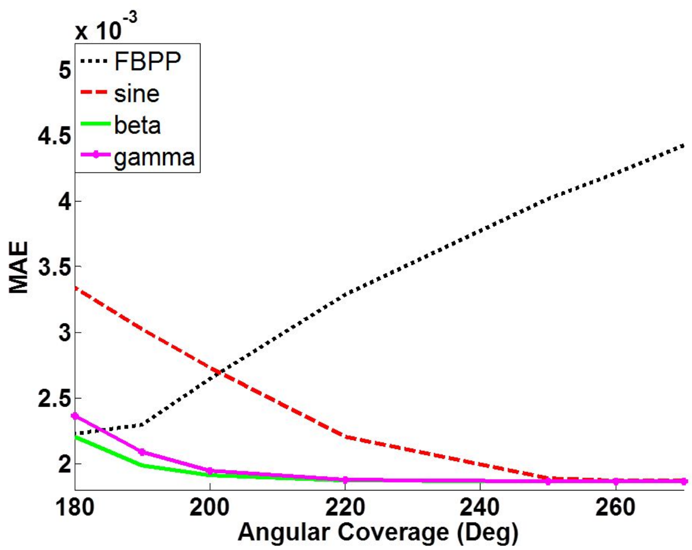

Figure 4.5: MAE calculated at different coverages for real part of reconstructed image with regular FBPP and MS-FBPP using different weights

4.3 Summary

In this part of the thesis, new approach to exploit data redundancy within the traditional 2D DT setup has been explored. Using cumulative distribution functions, especially the beta-cdf, it was shown that distortionless reconstructions of complex-valued object func-

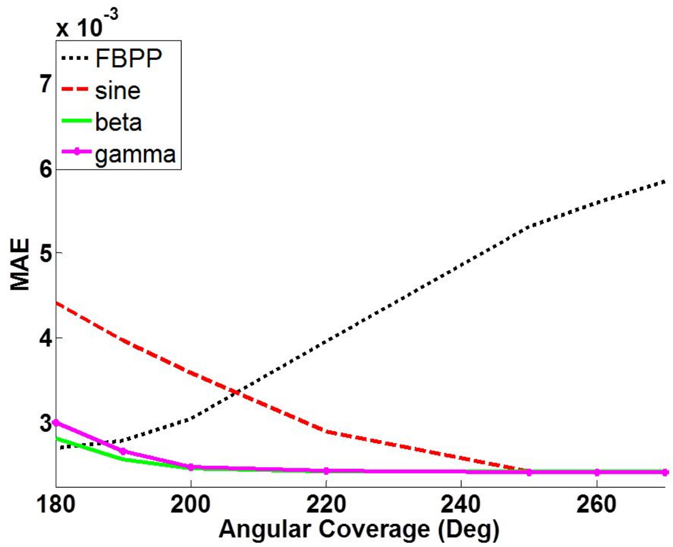

Figure 4.6: MAE calculated at different coverages for imaginary part of reconstructed image with regular FBPP and MS-FBPP using different weights

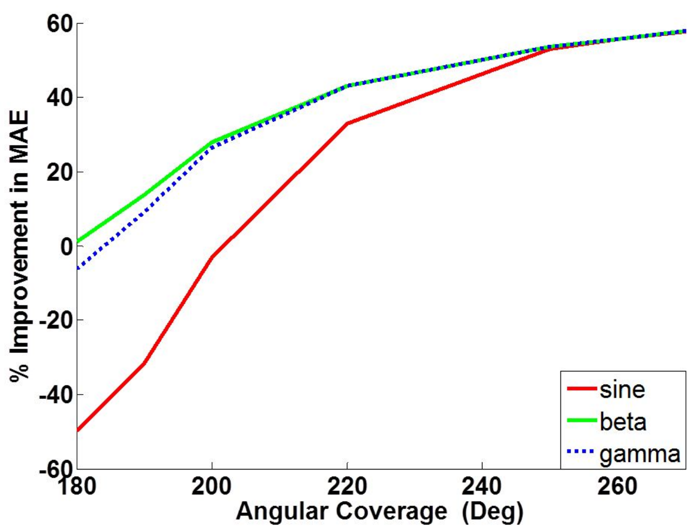

Figure 4.7: Percentage improvement of MAE from different weights over regular FBPP at different coverages for real part of reconstructed image

tions are possible even at angular coverage of 200°. The advantages of this observation are numerous. The major benefit is that it reduces the angular scanning requirements for accurate reconstructions. This also implies shorter access times for collecting relevant projection data. In medical applications this can mean a lower amount of exposure to

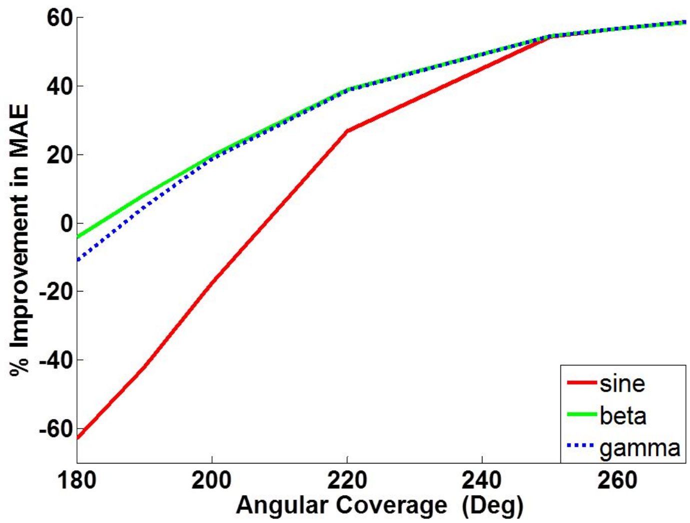

Figure 4.8: Percentage improvement of MAE from different weights over regular FBPP at different coverages for imaginary part of reconstructed image

the interrogating energy and also, fewer artifacts due to temporal variations caused by movements of the patient. For still lower coverages ($< 180^\circ$), the redundancy in the tomographic dataset vanishes and alternate approaches are being explored for application to DT setups. In the next part of the thesis, reconstruction algorithms under the compressed sensing regime have been developed. These fall under iterative techniques and the aim is to solve an optimization problem, the solution of which is in agreement with the available projection data. So, these are not fast one-step reconstructions as those of this first part of the thesis, however, at the cost of algorithmic complexity very sparse or highly limited data requirements can be achieved for full image recovery. This is the topic for the next part of this thesis.

Part 3

Reconstruction from highly limited projection data: Compressed sensing approach

Chapter 5

Overview

Recently a huge thrust area of research has been in the so called 'compressed sensing' regime [1, 41–43]. The strength of this area is that it has given a firm mathematical background and structure which ensures very low error guarantees to solutions from highly under-determined systems. It is a radically new way of sampling and recovering signals at sub-Nyquist rate. The traditional bounds put by the Shannon-Nyquist theorems can be defeated under certain conditions. Fortunately these conditions are met in a number of imaging and sensing applications. Hence compressed sensing becomes a very important new realm of signal sampling and recovery.

This chapter gives a brief background and introduction to this emerging field. The importance of compressed sensing for medical imaging is also described. The motivation to use this framework for microwave imaging is explained. The proposed framework and approaches are presented in the succeeding sections.

5.1 Background

Traditionally, any analog signal reconstruction is limited by the Shannon-Nyquist theorem which puts a lower limit on the minimum amount of information required for reconstructing the signal exactly [44]. When a signal is sampled, this theorem states that the sampling rate must be at least twice the highest frequency present in the sampled signal. This is known as the Nyquist rate which provides theoretical limits on sampling requirements. This implies that higher the frequency components in the sampled signal, larger the number of samples or measurements necessary to retain adequate information. This in turn implies higher time and acquisition complexity. However, recently it was found that under certain conditions signals can be sampled at rates much lower than the Nyquist requirement without any significant loss of information [43,45–47]. This remarkable possibility is largely due to the fact that for most practical signals, of bandwidth say B, all the components within the range B do not have equal amount of information. Thus the sampling frequency dictated by the Nyquist theorem is much higher for many practical signals. Compressed sensing has effectively exploited this loophole with great success.

The field of compressed sensing was triggered by two ground breaking papers by Donoho [43] and [45] and followed by a host of follow up papers which mathematically formalized the theory. The field benefited from fruitful combination of theories in applied mathematics, statistics and electrical engineering with applications in different disciplines ranging from image processing [48], radar technology [1], sampling theory [49], medical imaging [50]. In fact [50] opened up the CS theory as a great tool for medical imaging. MRI proved as a great field to demonstrate the potential benefit of CS and a considerable volume of work followed on CS based MRI reconstruction: [51–55] etc. to mention a few. Soon a huge interest was generated in applying CS to different medical imaging schemes and tomography in general: [56–60] etc. The available literature proves the usability of the CS framework for tomographic reconstructions. The aim of this research is to setup a CS framework to reconstruct complex-valued object function from limited angular projection data in diffraction tomography.

5.2 CS Theory

Compressed sensing aims to reduce the number of minimum measurements required to completely describe a signal by exploiting its *compressibility*. This can be expressed in terms of sparsity of a signal. A S-sparse signal $f \in R^n$ is a signal which has at most S non-zero elements. The goal is to be able to completely reconstruct a S -sparse signal f of dimension n from M measurements where $M \approx S$ or marginally more. To do this, the measurement (or data acquisition), signal handling and image recovery (reconstruction) has to be done in a certain framework and adhering to some constraints. These are actually the very conditions which enable us to defeat the Shannon sampling rate on a grand scale. These requirements are briefly enumerated below:

- The signal of interest f should be sparse or compressible in some domain.

- A stable measurement matrix Φ must be available which can transform the sparse signal, $f \in R^N$ to $y \in R^M$ without any loss of information due to the dimensional reduction from N to M. This condition of Φ is often referred to as the Restricted Isometry Property (RIP).

- A reconstruction algorithm which can recover the original signal from the measurements y. For compressed sensing framework, l_1-norm minimization is the de-facto algorithm of choice.

These properties and requirements are discussed next. A curious fact is that many physical signals of interest do in fact abide by these conditions. Hence, compressed sensing is applicable to a variety of scenarios. Thus, the development of this new theory gained a huge impetus over the last few years. It has become one of the most hotly researched topics under image reconstruction algorithms.

5.2.1 Sparse Basis Representation

In the present world, information travels over the internet at an enormous rate. Large volumes of data are stored in servers across the world. All this would really have not been possible without the available data compression techniques. A huge amount of research has been done in this area. The most famous works in this aspect are probably the wavelet transforms and discrete cosine transforms (DCT), see e.g. [61, 62]. These techniques are routinely used for reducing storage of large images. This is done by exploiting sparsity of images in these bases. Another very important sparse representation is the image gradient. In many practical cases, especially in medical images, the images themselves are not sparse, however, their gradient magnitude image or GMI is sparse. Wavelets are a great example of sparse basis set for images. This means that when an image is transformed to its wavelet domain, only a very few coefficients in that domain have non-zero or significantly high values. So, if these coefficients are thresholded, the resulting vector of coefficients is sparse with practically no lost information. To state it mathematically, consider a signal vector $x \in R^N$ which could be an image with N pixels. Let it be expressible in some orthonormal basis $\Psi = [\psi_1, \psi_2, ...\psi_n]$, such that:

$$x(t) = \sum_{i=1}^{N} s_i \psi_i(t), \tag{5.1}$$

where $s_i =< x, \psi_i >$, are the coefficients of x in Ψ domain. Here, t is the time index or pixel location depending on whether the x is a time signal or picture. Then x can be readily expressed as

$$x = \Psi s, \tag{5.2}$$

where s is the coefficient sequence. Ψ is a matrix with $\psi_1, \psi_2, ...\psi_n$ as columns. Now the importance of sparsity can be explained as follows: since Ψ is a sparse basis of x, the low valued coefficients of s can be discarded without much loss of information (or image quality). Let $x_k(t)$ be the recovered signal by keeping the K largest coefficients of s, i.e., $x_k := \Psi s_k$ where s_k is the coefficients' vector (s_i) with all but K highest coefficients set to 0. This vector s_k is sparse because only a few of its entries are non-zero, i.e. $K << n$. In literature, a vector like s_k is called K-sparse, meaning there are at most K non-zero entries in the entire vector s_k. Ψ being an orthonormal basis, the following relation holds:

$$\|x - x_k\|_2 = \|s - s_k\|_2. \tag{5.3}$$

If the sorted magnitudes of s decay very rapidly, then s_k and s would be almost equivalent. Thus, the error $\|x - x_k\|_2$ would be small and x_k would be a very accurate approximation of x. As an example, in Fig. 5.1 the loss due to rejecting $> 95\%$ of the coefficients in the wavelet domain is visually almost imperceptible. On the left is the original gray scale image and a zoomed-in section. On the right, the corresponding

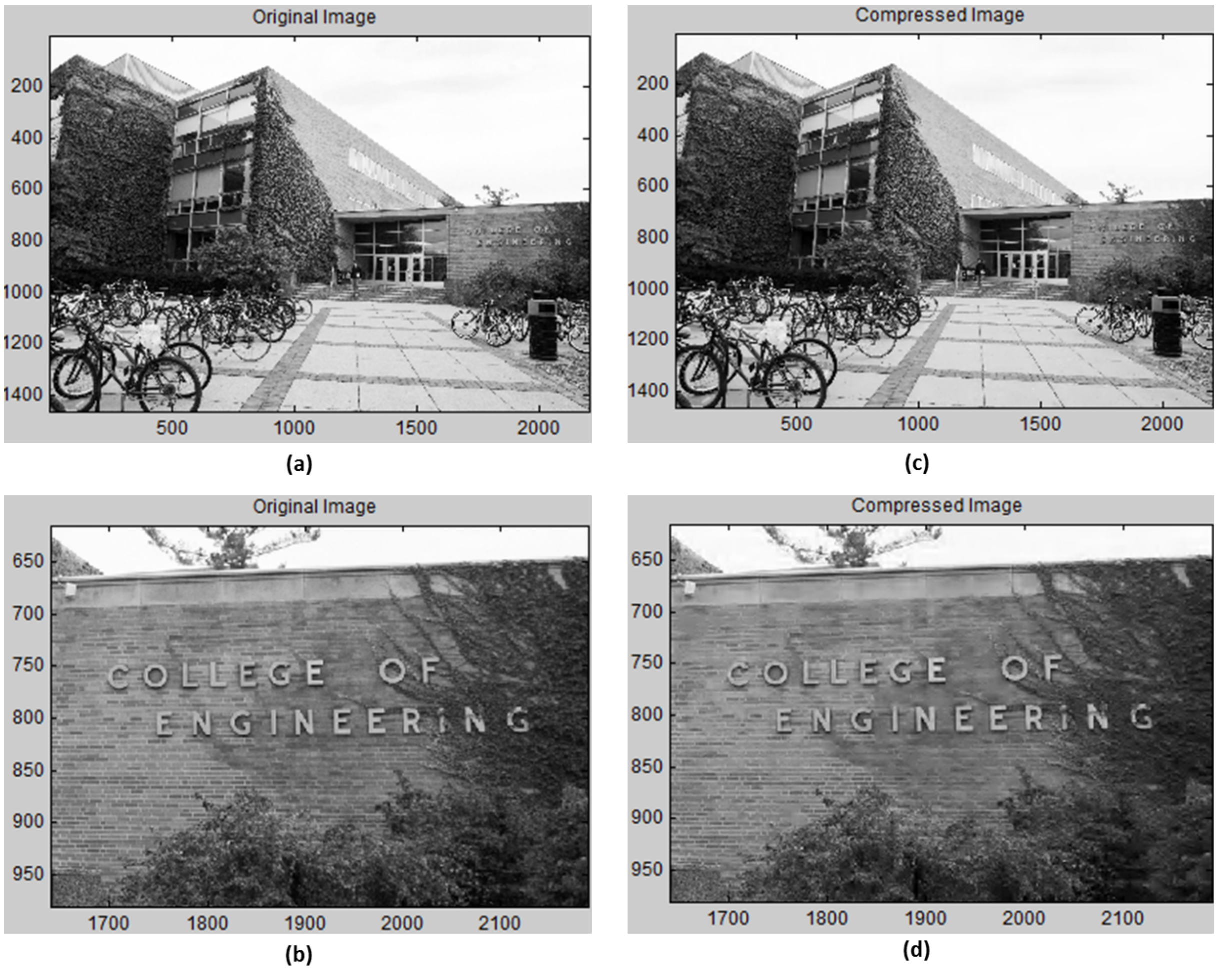

Figure 5.1: (a) Sample image (b) zoomed-in view (c) Compressed image by retaining $< 5\%$ of largest coefficients in wavelet domain. (d)zoomed-in view of the compressed image

compressed images (compressed in wavelet domain) are shown. This demonstrates that even though the original image by itself is not sparse, it can be effectively sparsified in some suitable domain. Then with respect to this domain, the number of required measurements (in our case, projection data) would be far less than in the original case. A point to note here is that compressed sensing only claims to reconstruct *sparse* signals. So in effect the sampling theorem is not really violated. However the main challenge is to identify the sparsity domain and then design an effective sampling and reconstruction system.

5.2.2 Sensing Matrix: The Restricted Isometry Property

Consider a sensing matrix Φ, representing the data acquisition. For example, in tomography, Φ is the Fourier matrix. Let Φ directly compress the signal while *sensing* it. That is, a small number of measurements (e.g. projection data in tomography) retain all the information within the original signal. Let it be a linear measurement process that collects M datapoints ($M < N$). Then Φ is a $M \times N$ matrix and the output y is an inner product of x with the columns of Φ. Then using (5.1), we can write

$$y = \Phi x = \Phi \Psi s = \Theta s. \tag{5.4}$$

where $\Theta := \Phi\Psi$ is an $M \times N$ matrix. The measurement or *sensing* matrix Φ is fixed and independent of x. In traditional theory, since $M < N$, the system in (5.4) is under determined and in general the solution is ill-posed. However, the sparsity of x in the Ψ domain alleviates this issue. The necessary and sufficient condition for this $M \times N$ system to have guaranteed stability is the following: if for any vector v which has $3K$ sparsity, if the following relation holds:

$$1 - \epsilon \leq \frac{\|\Theta v\|_2}{\|v\|_2} \leq 1 + \epsilon, \tag{5.5}$$

then a stable inverse exists for all K-sparse and compressible signals. This is the so called Restricted Isometry property or simply RIP. It might be an appropriate to introduce the formal definition of RIP here.

Definition: For each integer $k = 1, 2, ...,$ define the isometry constant $\delta_k \geq 0$ of a matrix

Φ as the smallest number such that

$$(1 - \delta_k) \|v\|_2 \leq \|\Theta v\|_2 \leq (1 + \delta_k) \|v\|_2 \,, \tag{5.6}$$

holds for all k-sparse vectors v. A matrix Φ has the RIP of order k as long as δ_K is *not too close to one* [41]. It can be surmised that when the RIP holds for Φ, then for K sparse signals, Φ will approximately preserve the Euclidean distance during sensing (or acquisition). This further means that the K-sparse vectors cannot be in the null space of Φ. This is because, if there is a K-sparse vector in the nullspace of Φ, then $\Phi x = 0 \Rightarrow \|\Phi x\|_2^2 = 0$. Then in (5.6), we must have $\delta_k \geq 1$, which goes against the definition of RIP where $\delta_k < 1$. This is beneficial as otherwise, there would be no way of preserving these signals. An important corollary is that if Φ satisfies RIP for K-sparse signals, then the solution x^* to the system $y = \Phi x$ can be recovered and further, the sparsest solution to the system is unique and the exact solution [63].

5.2.2.1 Incoherent sampling

Stability of the reconstruction can also be ensured by another approach. If the measurement matrix Φ can be ensured to be incoherent with the sparse basis Ψ, i.e. The columns of Ψ cannot be represented by linear combinations of columns of Φ and vice versa, then Φ and Ψ are said to be incoherent. An intuitive example would be impulses (delta function) for ϕ_i and Fourier sinusoids for ψ_i. Formally, coherence between the sensing matrix Φ

and sparse basis Ψ is defined as

$$\mu(\Phi, \Psi) = \sqrt{N} \max_{1 \leq k,j \leq N} \quad |< \phi_k, \psi_j >| \, . \tag{5.7}$$

Coherence gives an estimate of the correlation between the two matrices. So, for a good sensing matrix, the correlation with the sparsifying matrix should be minimum , i.e. μ should be small. The range for μ is: $\mu(\Phi, \Psi) \in [1, \sqrt{N}]$. The upper limit is a result of the fact that the inner product $|< \phi_k, \psi_j >| \leq 1$ for two unit vectors. The lower limit is due to Parseval's rule, where, for each j, $\sum_{k=1}^{N} |< \phi_k, \psi_j >|^2 = || \psi_j ||_2^2 = 1$, [41]. A very simple example of such an incoherent pair would be the *spike basis* Φ with $\phi(k) = \delta(t-k)$ and Ψ the Fourier basis with $\psi_j(t) = n^{-1/2} e^{i2\pi jt/n}$. Here Φ can be viewed as the classical sampling scheme in time or space. The time-frequency pair gives $\mu(\Phi, \Psi) = 1$ providing maximum incoherence. This incoherence is not limited to one dimension, and valid for higher dimensions as well. In typical practical applications, random matrices are mostly incoherent with any fixed basis Ψ [41]. If an orthobasis is selected randomly from an uniform distribution (e.g. by sampling n vectors on the unit sphere independently and uniformly) and orthonormalized, then with high probability, the coherence between Φ and Ψ would be low and of the order of $\sqrt{2 \log n}$

To summarize, the sensing matrix Φ must have RIP property or be incoherent to the sparse basis Ψ for compressed sensing to be successful. However proving that a particular matrix Φ does indeed have RIP is an NP-hard inverse problem. Fortunately, some classes of matrices have already been proven to have RIP. If these matrices could represent particular sensing or data acquisition techniques, then the reconstruction can be performed under the compressed sensing regime. A very important category of RIP matrices is a *partial Fourier* matrix. A partial Fourier matrix is formed when the M rows of the matrix Φ are chosen randomly from a full $N \times N$ Fourier matrix. Then Ω satisfies RIP. This implies that the compressed sensing framework can be applied to tomographic reconstruction, as the projections in a tomographic acquisition are directly related to the Fourier or k-space of the object being probed. This has in fact generated a huge interest in applying CS techniques for image recovery from highly sparse tomographic data.

5.2.3 Image Reconstruction

The RIP gives theoretical guarantee that a K-sparse signal can be fully recovered from M measurements given by the measured vector y. However,the recovery process has not been addressed there. The recovery procedure should be able to regenerate the N-length signal x or the sparse representation s, when y, Φ and Ψ is given. We have $M < N$ in 5.4. So there are in theory infinite solutions, the solution space given by a (N-M) dimensional hyperplane, $\mathcal{H} := \mathcal{N}(\Theta) + s$ in R^{N}, which is the null-space $\mathcal{N}(\Theta)$ of Θ translated by the true solution s. This happens since $y = \Theta(s) = \Theta(s+r)$ for $\forall\ r \,\epsilon\, \mathcal{N}(\Theta)$. The requirement and challenge then becomes one of finding the sparse signal s in the translated null space.

5.2.3.1 *l*-2 Minimization

The classical approach to handle this type of inverse problems is by means of a least-squares method. Here, the vector in the translated nullspace $\mathcal{H}$ with smallest l_2 norm (i.e. minimum energy) is selected:

$$\hat{s} = \text{argmin} \mid\mid s' \mid\mid_2, \text{ such that } , \Theta s' = y. \tag{5.8}$$

The advantage of this method is in the availability of a closed form solution of the form: $\hat{s} = \Theta^T(\Theta\Theta^T)^{-1}y$. Unfortunately what is being sought is a K-sparse vector. Minimizing the energy does not help as the sparsest signal is not bound to have minimum energy as well. l_2 minimization is not a sparsity promoting method. As a result, what is recovered is a non-sparse low energy signal which is not the true solution.

5.2.3.2 *l*-0 Minimization

Since l_2 minimization does not promote signal sparsity, a logical alternative is to locate the sparsest vector in the translated null space $\mathcal{H}$. That is to perform a l_0 minimization:

$$\hat{s} = \text{argmin} \mid\mid s' \mid\mid_0, \text{ such that } , \Theta s' = y. \tag{5.9}$$

As was mentioned before, it has been shown that this can generate the exact solution for a k-sparse signal from $M = K + 1$ measurements [64], [63] which makes the scheme attractive. However, solving (5.9) is numerically unstable with computational complexity of an NP-complete problem which requires exhaustive enumeration of all $\binom{N}{K}$ possible combinations to find the non-zero entry locations in s.

5.2.3.3 *l*-1 Minimization

A surprising fact in compressed sensing field is that in many of its relevant practical problems, a l_1 norm can replace the l_0 norm in the minimization scheme described above to get equivalent and stable reconstructions with high probability. Most of the signal recovery related work in compressed sensing explores the use of l_1 as a substitute of l_0 norm. In [42], it was shown that for a k-sparse signal, if the measurement size M satisfies

$$M \geq cK \log(N/\delta), \tag{5.10}$$

then with probability more than $1 - \delta$, the solution to the l_1 minimization problem:

$$\hat{s} = \text{argmin} \parallel s' \parallel_1, \text{ such that }, \Theta s' = y, \tag{5.11}$$

is the required original signal. In the presence of noise, the constraint is just $\parallel \Theta s' y \parallel_2 \leq \varepsilon$ with ε being a tolerance parameter. The l_1 minimization problem can be recast as a convex optimization problem as:

$$\hat{s} = \text{argmin}_{\hat{s} \epsilon R^{\text{N}}} \parallel y - \Theta s' \parallel_1 . \tag{5.12}$$

This can be conveniently solved as a linear program called *basis pursuit*, which has $O(N^3)$ computational complexity [45], [43]. A very well researched minimization problem is to minimize the following functional:

$$F_\tau(x) \equiv \parallel \Phi x - y \parallel_2^2 + 2\tau \parallel x \parallel_1, \tag{5.13}$$

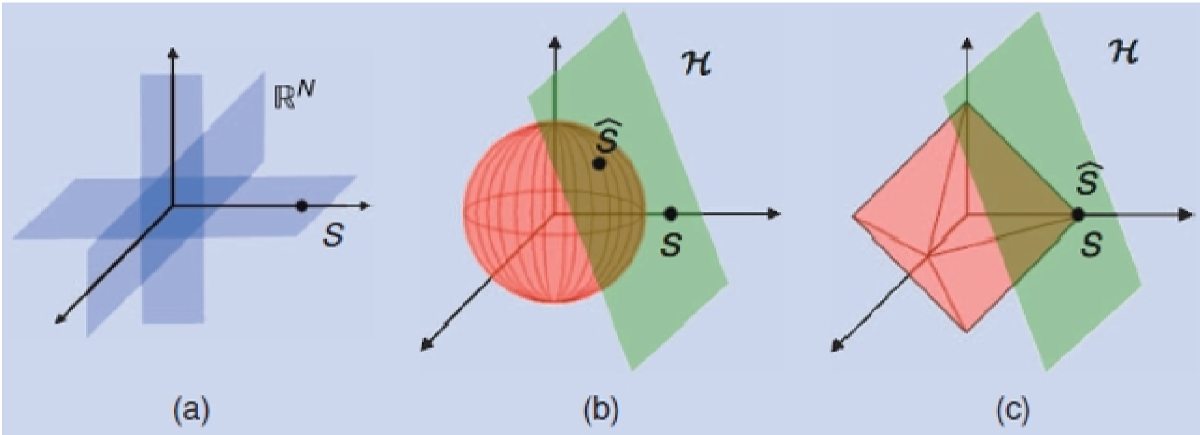

Figure 5.2: Visual interpretation of the effectiveness of different norms for signal recovery by minimization [1]: (a)A sparse vector s lies on a K-dimensional hyperplane aligned with the coordinate axes in R^N and so close to the axes (b) Recovery through l_2 minimization does not find the correct sparse solution on the translated nullspace (green hyperplane), but a non-sparse solution $\hat{s}$ with least energy. (c)With sufficient measurements, recovery by l_1 minimization does find the correct sparse solution s.

with $\tau > 0$. This is an unconstrained convex optimization problem. It has been shown [65] that a solution to (5.11) would also minimize (5.13). Thus many well investigated convex optimization algorithms can be applied to solve a l_1 minimization problem.

5.2.3.4 Geometrical Insights

A geometric viewpoint gives a simpler intuitive explanation as to the effectiveness of using the l_1 norm over the l_2. For the graphical representation, Fig 5.2 is used from [1]. The set of all K-sparse signals s in a N-dimensional space (R^N) is a non-linear space consisting of K-dimensional hyperplanes aligned with the coordinate axes (shownn in Fig. 5.2(a)). Then, sparse vectors are located near the co-ordinate axes in R^N.

When l_2 minimization is performed, the translated nullspace $\mathcal{H} = \mathcal{N}(\Theta) + s$ has dimension $(N - M)$. It is oriented at a random angle due to the randomness in Θ as shown in Fig. 5.2(b)). A point to note here is that in reality, $N, M, K >> 3$ and hence some intuitive imagination is required to view the same in higher dimensions.

The l_2 minimizer $\hat{s}$ of (5.11) is the point on $\mathcal{H}$ nearest to the origin. As $\mathcal{H}$ has a random orientation, with a high probability $\hat{s}$ will be neither sparse nor near to any coordinate axes and hence to s.

Any l_p minimization scheme (where $p = 0, 1, 2...$, etc.) can be geometrically viewed as progressively enlarging the l_p ball from the origin till it touches the constraint hyperplane ($\mathcal{H}$). The point of contact gives the minimizer of that l_p problem. The general definition of the l_p unit ball is:

Definition- The l_p unit ball $\mathcal{B}$ of a vector space V is the set of all vectors with l_p norm less than or equal to one, i.e.

$$\mathcal{B} = \{x \in V \quad | \quad || \, x \, ||_{\mathrm{p}} \leq 1\}. \tag{5.14}$$

The l_1 ball is diamond shaped with the vertices aligned along the coordinate axes (Fig 5.2(c)). The spikiness along the coordinate axes increase with increasing N. So when the l_1 ball is blown outwards, it first touches $\mathcal{H}$ at a point near the coordinate axes which is where the actual signal s is located. Thus l_p minimization turns out to be a suitable sparsity promoting minimization scheme.

5.2.3.5 Summary

In short, what is seen is that to set up a compressed sensing based system, one has to come up with a data acquisition scheme from random measurements. The sensing matrix Φ must have some specific properties as discussed.After acquisition, signal is recovered through linear programming reconstruction scheme. The error term to minimize would ideally be the l_0 norm but due to computational constraints, the alternative is to use the l_1 minimization. Fortunately the latter performs equally well under certain conditions mentioned earlier. These findings lead to a huge amount of research conducted on l_1 based reconstruction schemes under the compressive sensing regime. In the following chapters, the CS based framework for diffraction tomography will be described and results thus obtained will be presented.

Chapter 6

CS based Reconstruction for DT

The projection data acquisition in diffraction tomography (ref. chapter- 2) can be expressed as

$$F = \Phi(x) \tag{6.1}$$

where Φ is the diffraction operator, F is the sample data in k-space and x is the object function $x(r)$. If the acquired data is highly sparse, then classical interpolation methods are no longer applicable as the Nyquist limit is not met. FBPP alone results in a lot of artifacts in the reconstructed image and distort actual features in the image. Using more accurate non-uniform fast Fourier transforms, a compressed sensing framework can be set up,for high quality reconstruction from sparse view data. Firstly, it is assumed that x is approximately sparse in some domain Ψ, such that $x = \Psi s$ as in previous sections. Then, with the availability of F, knowledge of Φ and Ψ, we can formulate a convex optimization problem using the functional in (5.13):

$$\min_{s} \{\alpha \parallel s \parallel_1 + \parallel y - \Theta s \parallel_2^2 \}, \tag{6.2}$$

where α is the regularization parameter.

6.1 Application of CS to sparse DT recovery

For ultrasound or microwave based DT, the data acquisition matrix is the partial Fourier matrix. The sparse view data is generated by randomly choosing view angles. These samples give the vector y of (5.11) and (6.2). For setting up the CS framework, the sensing matrix $\Theta = \Phi\Psi$ must be constructed with Ψ being the sparse basis for the object. Let the object function be denoted by f, so that $f(x, y)$ can be used to represent the spatial distribution of the object function. The object has a bounded support, say $[-C, C] \times [-C, C]$, i.e. $f(x, y) = 0$ for $|x|, |y| > C$. Let f_d denote the discretized object function which is to be reconstructed. $f_d \in \mathbb{C}^{n_d \times n_d}$, with $n_d = 2[C/T])$ with T being the sample period. Also, let $F(u, v)$ and $F_d(u, v)$ be the Fourier transforms of $f(x, y)$ and $f_d(n_1, n_2)$ respectively. Also, the receiver array will have limited number of elements. Let the discrete field be $\hat{u}_{s,\theta} = u_{s,\theta}(n\tau)$, where τ being the spatial sampling interval of the system. Let $\hat{U}_{s,\theta}(\kappa)$ and $U_{s,\theta}(\kappa)$ be the respective Fourier transforms. In the limit $\tau \to 0$, both the signals become equal. A point to note here is that the Fourier transform of the scattered field is related to the Fourier space of the object along semicircular arcs as mentioned in section 2. Here, κ gives the projection of a point on the semicircular arc to its tangent at the origin. Also, θ is the angle of incidence. Then, invoking the FDP, we can have $\hat{U}_{s,\theta}(\kappa) \approx U_{s,\theta}(\kappa) = F(u, v) \approx F_d(u, v)$. Let $\Omega_1 = \theta_1, \theta_2, .., \theta_{N_1}$ be the set of view or projection angles over which $\hat{u}_{s,\theta}(n\tau)$ is obtained and from that $\hat{U}_{s,\theta}(\kappa)$ is calculated for $\forall\kappa \in \Omega_2 = \kappa_1, \kappa_2, ..., \kappa_{N_2}$. Then, f_d can be reconstructed from the projection dataset

$\hat{U}_{s,\theta}(\kappa) \mid (\theta, \kappa) \in (\Omega_1, \Omega_2)$ as [66] :

$$\frac{(T\kappa_0)^2 U_0}{2j\gamma} e^{j\gamma l} \sum_{n_1=\lfloor -C/T \rfloor}^{\lceil C/T \rceil} \sum_{n_2=\lfloor -C/T \rfloor}^{\lceil C/T \rceil} f_{d_{n_1,n_2}} e^{-2\pi j(n_1 u + n_2 v)T} = \hat{U}_{s,\theta}(\kappa) + n_{s,\theta}(\kappa). \quad (6.3)$$

This is expressible in a compact matrix equation form as $\Phi f_d = F + n$, where $\Omega = (\Omega_1, \Omega_2), \Phi \in \mathbb{C}^{|\Omega| \times (n_d)^2}, f_d \in \mathbb{C}^{(n_d)^2}, (n_1, n_2) \leq |n_d/2|, F \in \mathbb{C}^{|\Omega|}$. From (6.3), the Φ for the minimization problem is obtained. Essentially, the summation expression in (6.3) gives the coefficients of a Fourier matrix. By FDPT, the spatial frequency samples are gathered along the arc AOB (see Fig. 2.1). As the angle of incidence varies, the arc revolves around in the Fourier space and describes a centered disk of radius $\sqrt{2}k_0$. So the reconstruction of the object is always a low-pass filtered version of the original image. The following steps would be used to assure that the CS framework is maintained:

- **Incoherence** will be maintained by using a random set of angles for the projection data. A partial Fourier matrix will be used, which ensures RIP of the sensing matrix.

- **Sparsity** will be exploited initially through image gradients in section-7.1. Later, in section-7.2 simultaneous exploitation of multiple sparse domains will also be explored briefly.

Let the sparse basis matrix be Ψ. Combining l_1 norm and data constraints in the minimization problem, the initial problem is of the form:

$$\min_s \{G(s) = \| F - \Phi\Psi s \|_2^2 + \alpha \| s \|_1 \}. \quad (6.4)$$

Here, F gives the spatial frequency samples, s is the coefficients of f_d in the sparse basis Ψ. In the next section, the reconstruction algorithm from projection dataset is presented.

6.2 Reconstruction

A minimization problem involves reducing a cost function in a series of iterative steps starting from an initial value of the cost function. The key feature is how the cost function is updated at each iteration. A significant amount of literature on methods are available to minimize a cost function. In this research, as the minimization problem is essentially a convex optimization problem, optimization toolkit from Boyd and Vanderbeghe [65] has been used.

The overall reconstruction algorithm sequentially follows these steps:

- Generate projection data from random view angles.
- Fourier space data along semi-circular trajectories is found applying the FDPT.
- Iterative reconstruction through l_1 minimization in the sparse domain is applied while preserving the data constraints .

In the following chapter, reconstructions have been performed using TV as the l_1 norm of the sparse domain. The performance of the reconstruction under varying degree of limited data and angular access have been evaluated.

Chapter 7

Reconstruction with Total Variation as l_1 penalty term

Most physical samples investigated tomographically, do in fact possess piecewise continuous property distribution. Particularly, biological specimens would fall under this category, where regions over extended areas would have no variations but rapidly vary in certain confined areas, such as edges of organs or boundaries between different tissue. These images themselves are not sparse, however, their gradient images are sparse.

This is one form of sparsity that can be exploited in a CS framework. The gradient magnitude image (GMI) is defined in terms of derivatives in the vertical and horizontal direction of the image. Let $D^h_{n_1,n_2}$ and $D^v_{n_1,n_2}$ denote the finite difference operators in the horizontal (h) and vertical (v) directions respectively. The gradient of the image is $\nabla f_d = [D^h_{n_1,n_2}, D^v_{n_1,n_2}]f_d = Df_d$, where $D = [D^v, D^h] = \Psi$ is the sparsity promoting operator. The gradient magnitude then becomes $\mid \nabla f_d \mid = \sqrt{(D^h_{n_1,n_2}\ f_d)^2 + (D^v_{n_1,n_2}\ f_d)^2}$.

The l_1-norm of the gradient image has often been termed as the total variation (TV) of the image, which then can be defined as

$$TV(f_d) = \sum_{n_1,n_2} \sqrt{(D^h_{n_1,n_2}\ f_d)^2 + (D^v_{n_1,n_2}\ f_d)^2}. \tag{7.1}$$

TV can be employed as a means to exploit sparsity of piecewise smooth objects. It has been already used as a regularizing term before e.g. [32]. TV can be effective in suppressing Gibbs effect while preserving edges [67]. To use TV as the l_1 norm, in the minimization problem of (6.4), the sparse signal s is the GMI, so that $s = D(f_d)$ where D is the sparsity operator and by definition, $\| D(f_d) \|_1 = TV(f_d)$. In this case, (6.4) becomes

$$\min_s \{G(s) = \| F - \Theta s \|_2^2 + \alpha \| s \|_1 = \| F - \Phi D^* s \|_2^2 + \alpha TV(f_d) \}, \tag{7.2}$$

with α being the regularization parameter for the TV term and $\Theta = \Phi D^*$. To avoid a zero denominator in the TV term, an approximation which is often employed is: $\| D_{n_1,n_2} f_d \| \approx \sqrt{(D^h_{n_1,n_2} f_d)^2 + (D^v_{n_1,n_2} f_d)^2 + \mu}$, where μ is a small positive number. The second term in (7.2) is the data constraint term added to keep the problem as an unconstrained optimization problem. The parameter α determines the relative weightage of the data constraint term and the l_1 penalty term. The value of α needs to be carefully chosen. In most cases this value would be application specific. A standard approach is to plot a response of the two terms in the minimization term with respect to the variation of α. A sweep of α over a large range would generally give insight towards an optimal value. Over the range of the sweep generally as α increases, the l_1-norm decreases whereas the error norm increases. A value of α is so chosen as to make the l_1 norm low enough without increasing the error norm. For the reconstructions performed here, the value of α has been fixed at 0.2. Once the reconstruction problem is set up in the CS framework as shown here, the l_1 minimization is an optimization problem in standard form. It is efficient to use an optimization toolkit if applicable. For solving convex optimization problems expressed in standard forms, a host of optimization toolsets are already available. In this work, the minimization problem of (7.2) is solved using a convex optimization toolkit cvx by Boyd & Vanderberghe, [65], [68]. A particular advantage of using this toolkit is that it can be used to solve the primal-dual problem with the Matlab based SeDumi toolkit [69]. The solution comes with a certificate of convergence in the form of the distance from the dual maximum and the duality gap. So the distance of the solution (i.e. minimum of the objective function achieved) from the theoretical lower limit is known.

7.1 Reconstruction with TV as l_1 minimizer

As part of the main aim of this research, reconstruction was performed on a complex-valued phantom structure similar to that in Part 2. To see the effectiveness of TV as the l_1 penalty term, two types of data variation could be analyzed. The first being the number of projections when the angular access is fixed. The second being the variation of total coverage for a fixed number of projections. In this exercise, the projection datasets have been fixed at 15, 20, 30 and 45 views. The angular coverage limits have been fixed at $180^\circ, 150^\circ, 120^\circ$ and 90°. In the figures below, reconstructions of real and imaginary part of the phantom are shown separately for these aforementioned variations. The effect of both type of variations on the reconstruction error have been presented separately.

In Fig.7.1 and Fig.7.2, reconstructions from 45 projections have been shown. It can be seen that for the first three coverages, the quality of the images is almost constant. At 90° coverage, the reconstruction starts showing considerable distortion. This is however not

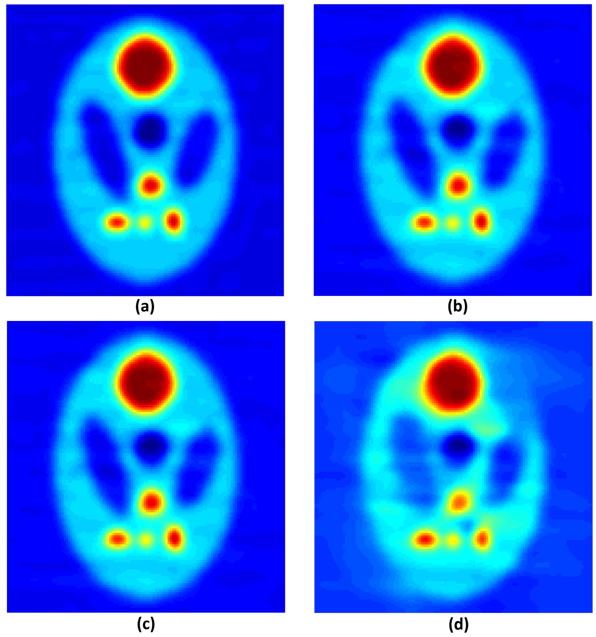

Figure 7.1: Reconstructions of real part of image with 45 views for different angular coverage of : (a) 180°, (b) 150°, (c) 120°, and (d) 90°

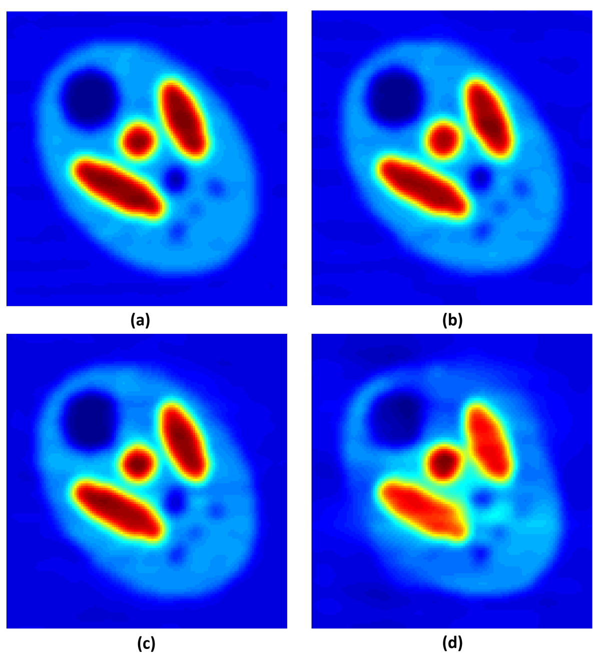

Figure 7.2: Reconstructions of imaginary part of image with 45 views for different angular coverage of : (a) 180°, (b) 150°, (c) 120°, and (d) 90°

surprising as the restriction of the available data has been limited on both grounds, that of projections as well as coverage. It is expected to see better reconstructions from same number of projections when the angular access is higher or more complete. The interesting observation here is that as the coverage decreases from $180°$ to $120°$, the degradation in the image quality is marginal and mostly would be acceptable based on the application. Detailed error analysis has been done in the next section of this chapter. From Fig.7.3 to Fig.7.8, the reconstructions of real and imaginary parts have been shown separately for angular sweeps as the number of projections is progressively decreased. With higher angular coverage, the reconstruction quality is maintained at upto 20 projections. Significant degradation is observed at 15 projections. This illustrates that as long as the coverage is high, the random sampling and l_1 minimization can perform good reconstructions from very few peojections. As the coverage is lowered, decent reconstruction is maintained at upto $120°$. For even lower coverage, the l_1 minimization alone is not effective. This is because the minimum data requirement even under sparse reconstruction starts to be violated.

7.1.1 Error Analysis

In order to quantitatively evaluate the reconstructions performed, the Mean Absolute Error (MAE) described in chapter 4 is used again. For error performance additional reconstructions for a coverage range of $60°$ has also been considered. The average error in reconstruction for real and imaginary parts have been calculated separately. The relative percentage change in MAE for different projection numbers and angular access are shown in Fig.7.9 - Fig.7.12.

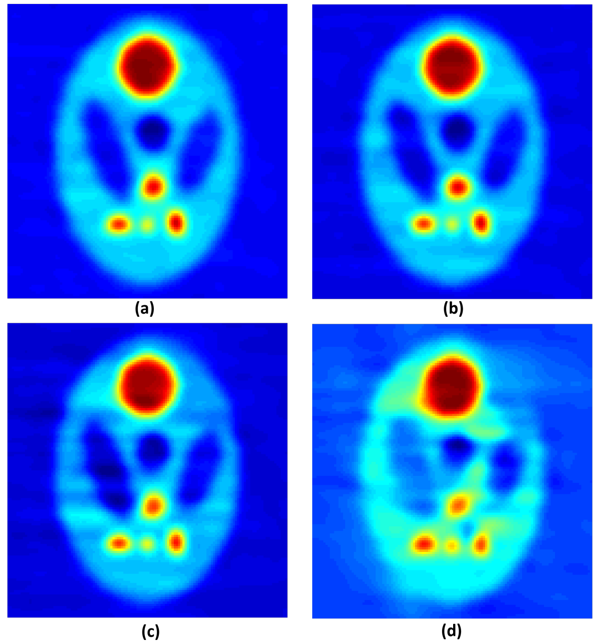

Figure 7.3: Reconstructions of real part of image with 30 views for different angular coverage of : (a) 180°, (b) 150°, (c) 120°, and (d) 90°

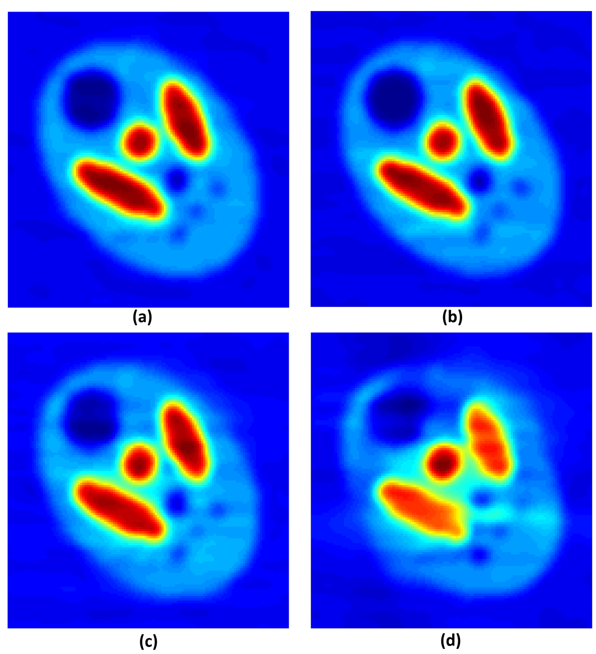

Figure 7.4: Reconstructions of imaginary part of image with 30 views for different angular coverage of : (a) 180°, (b) 150°, (c) 120°, and (d) 90°

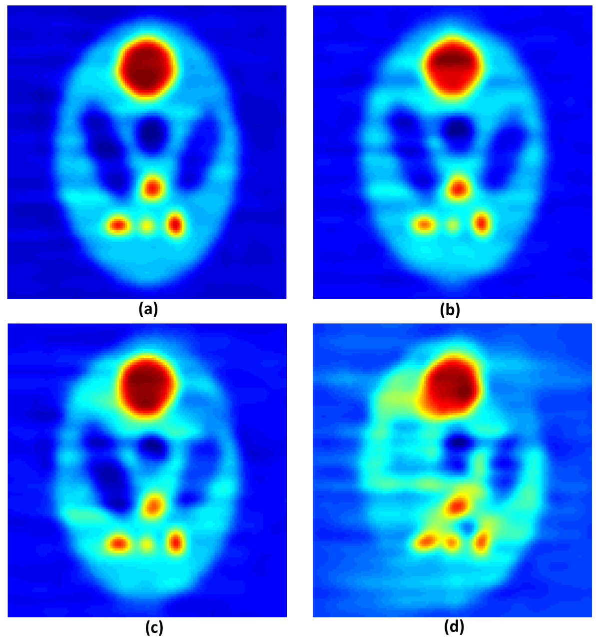

Figure 7.5: Reconstructions of real part of image with 20 views for different angular coverage of : (a) 180°, (b) 150°, (c) 120°, and (d) 90°

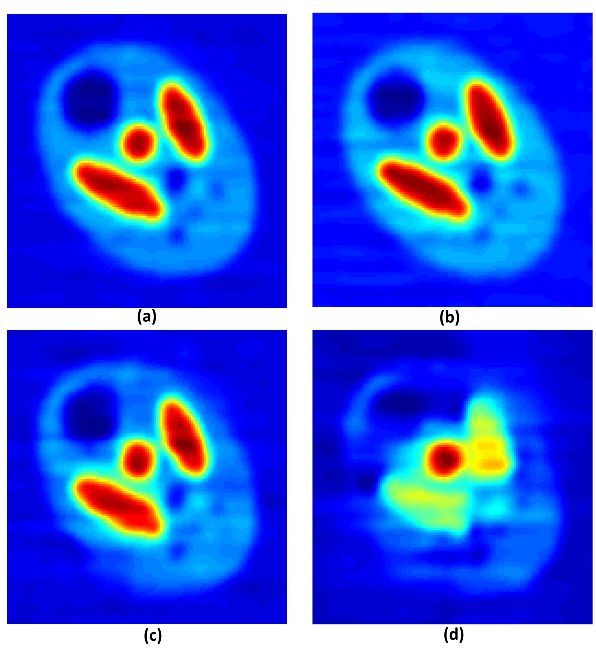

Figure 7.6: Reconstructions of imaginary part of image with 20 views for different angular coverage of : (a) 180°, (b) 150°, (c) 120°, and (d) 90°

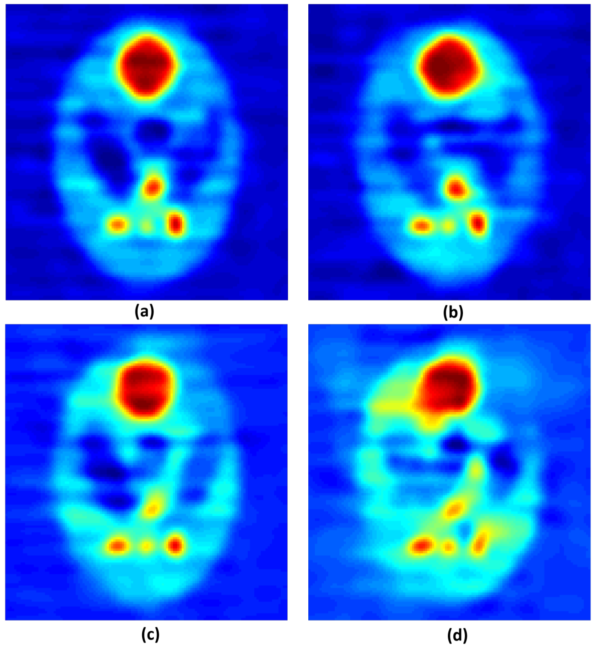

Figure 7.7: Reconstructions of real part of image with 15 views for different angular coverage of : (a) 180°, (b) 150°, (c) 120°, and (d) 90°

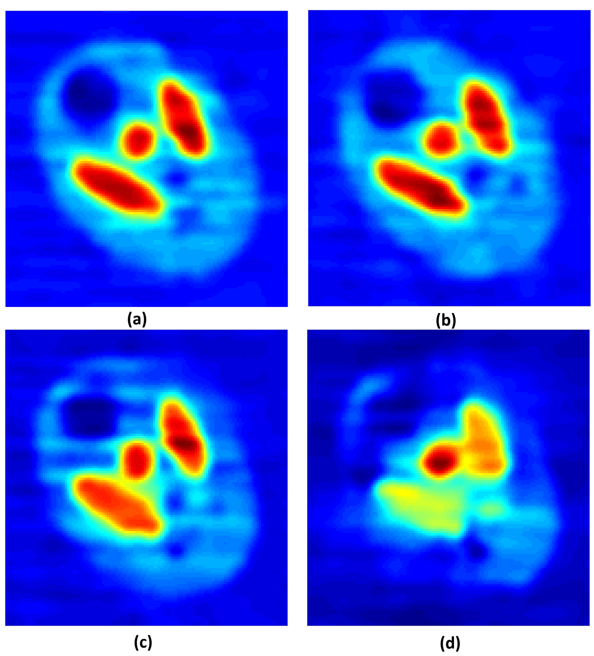

Figure 7.8: Reconstructions of imaginary part of image with 15 views for different angular coverage of : (a) 180°, (b) 150°, (c) 120°, and (d) 90°

Fig. 7.9 and Fig. 7.10 show the MAE increase for a fixed angular coverage as the number of projections change. The MAE from the maximum number of projections (60) is taken as the base reference to which the percentage change of error is measured as the number of projections is progressively lowered up to 15. This change is plotted for different angular coverages between 60° to 180°. Fig. 7.9 shows the performance for the real part of the reconstructed image and Fig. 7.10 for the imaginary part. As expected, for each angular coverage, as the available number of projections is reduced, the error increases, as seen from the plots.

The percentage increase remains below 20% for all coverages at 30 views. From 20 views or less, the error rate increases sharply, e.g. in the real part of the image, the MAE increase for 180° coverage at 20 views is 18% and 56.7% for 15 views. For 120° coverage, the values are respectively 26.7% and 43%. With respect to visual identification of features or defects from reconstructed image, this translates to good reconstructions maintaining all features upto 30 views and acceptable reconstruction at 20 views. At 15 views, the degradation gets considerably high to depend on the images for diagnosis or fault detection with high confidence. An important thing to note here is that in Fig. 7.9 and Fig. 7.10, each line show the percentage increase of error as the view number is decreased while the coverage is fixed. So, although all the plots start at 0% error increase, the actual error value would be higher for a lower coverage, and vice versa. The total coverage determines the extent of data availability for reconstruction. Hence, the change in percentage MAE increase is more striking for higher angular coverages than lower ones. This is illustrated through the plots themselves. The percentage change for 60^o is 10.5% in real and 12.4% in imaginary part at 15 projections which is the lowest change observed.

This is because the starting point itself is already much worse due to limited coverage and in effect does not get worse with lower number of projections. The observed percentage change in error increases with increasing angular coverage. The MAE plots show that with higher access, the reconstruction accuracy increases.

Another avenue to explore is to observe the effect of the available angular access for a fixed number of projections. This effect is illustrated in Fig. 7.11 and Fig. 7.12. Here, for a fixed number of projections, the percentage MAE error is calculated with respect to the maximum angular coverage (180°). The coverage is decreased to 60°. The process is repeated while varying the number of projections from 60 to 15. A similar trend is observed as in the last case. For each fixed projection number, the MAE error increases as the total coverage decreases. This is expected. However, a surprising and appealing fact is that the increase in error is marginal irrespective of total number of projections between 180° to 120°. This illustrates the stability and utility of this CS based reconstruction procedure. The procedure would be handy in either lower angular access or a sparse projection dataset (and upto a certain limit when both constraints are simultaneously present). This puts this CS based framework in a strong position to handle highly adverse data acquisition conditions.

In summary from these reconstruction sets it can be concluded that at 120° coverage, as little as 20 projections might be sufficient for a reasonably accurate reconstruction. This is definitely a great improvement over other traditional iterative methods.

Further restrictions would be too limiting for reconstruction in a generalized setup of complex valued image with no prior information or known restrictions. However when we have some a-priori knowledge, either about the structure or some practical insights about the imaged system or ROI, tighter bounds might be achievable as will be demonstrated briefly in the next subsection.

7.1.2 Reconstruction from phantoms with realistic permittivity distribution

In practical scenarios, the physical distribution of permittivity variation in the real and imaginary parts would be same, i.e. the real and imaginary parts of the complex valued image would have the same spatial variations and would essentially look same. In this section some reconstructions from a more realistic phantom is shown. The imaginary part of the phantom is kept same as the real with respect to the shape, as expected in practical measurements. Thus the data requirement would be looser than in the last section. Reconstructions from 15 and 10 projections from different angular coverage are given in Fig. 7.13 - Fig. 7.16. As is evident, for 15 views, there is almost distortionless reconstruction for all angles. The imaginary part shows more degradation than the the real part at lower coverage. This is because the magnitude of the imaginary components have been kept at half of that in the real part and as such, is more susceptible to degradation in general and especially under sparse data recovery conditions. For 10 views, the real part is well retained upto 120°, however, below 150°, the imaginary part degrades considerably. In conclusion, we see that for 15 projections, acceptable reconstruction can be achieved at 120° and for 10 views at 150°. At full 180°, even 10 views can generate a clear reconstruction, maintaining all features distinctly. For any measurement system, noise is an integral part. The robustness of any reconstruction algorithm is dependent on the noise

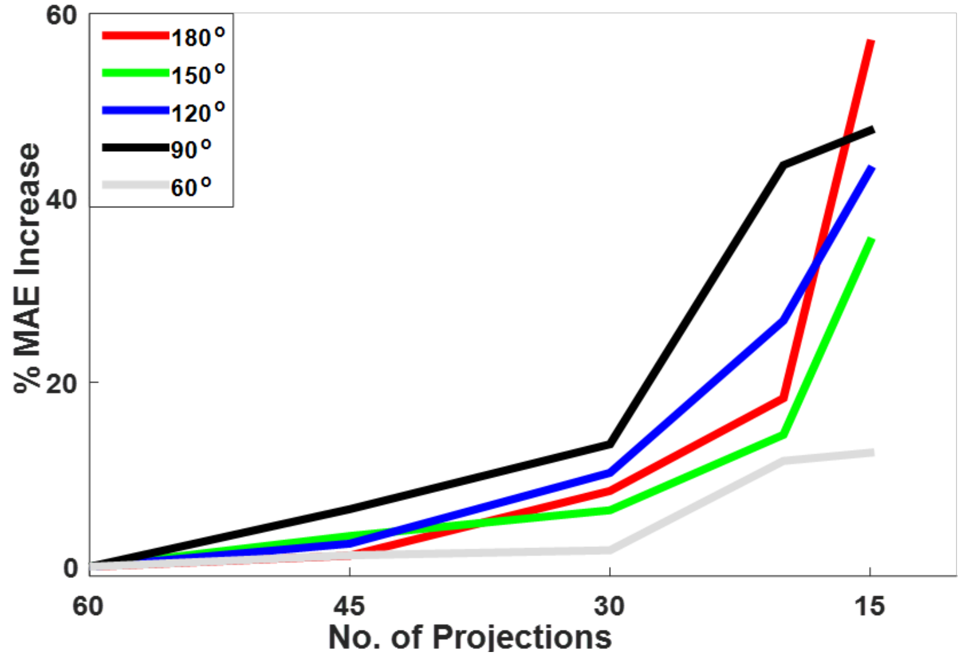

Figure 7.9: Percentage increase of MAE for real part of image as the coverage is lowered for a fixed number of projections. Graphs plotted for different number of projections

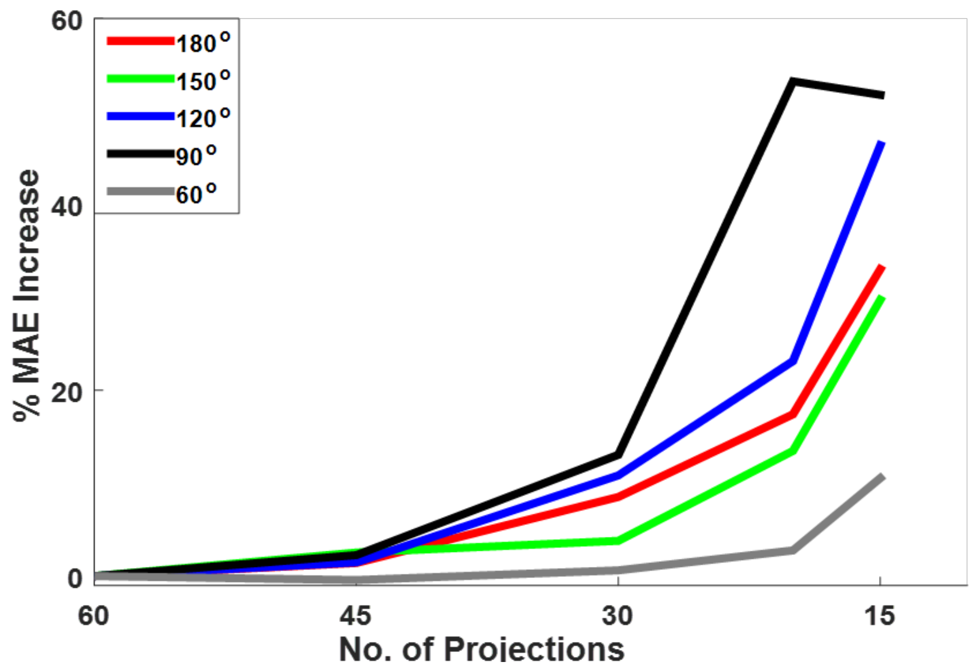

Figure 7.10: Percentage increase of MAE for imaginary part of image as the coverage is lowered for a fixed number of projections. Graphs plotted for different number of projections

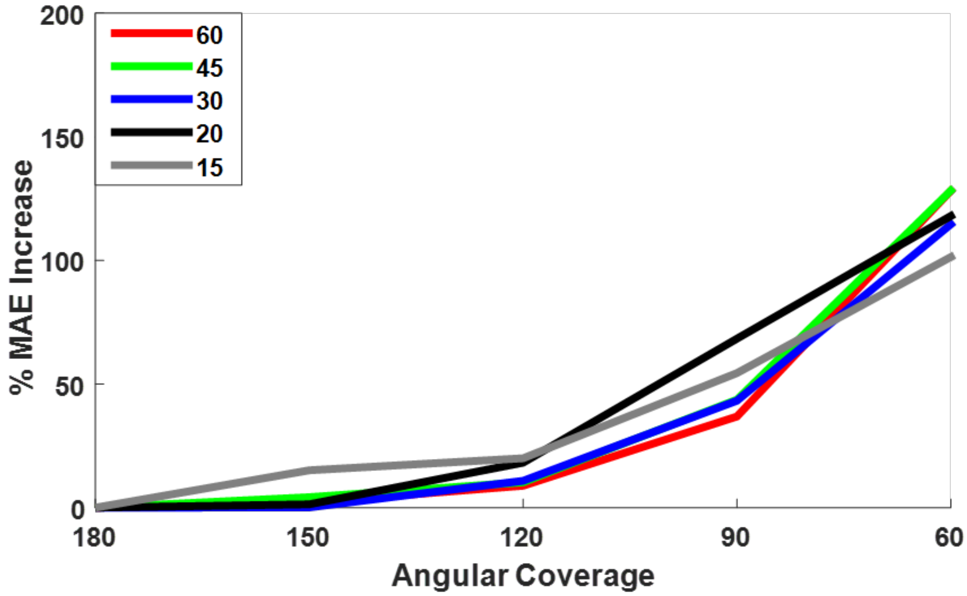

Figure 7.11: Percentage increase of MAE for real part of image as the number of projections is lowered for a fixed coverage. Graphs plotted for different coverages

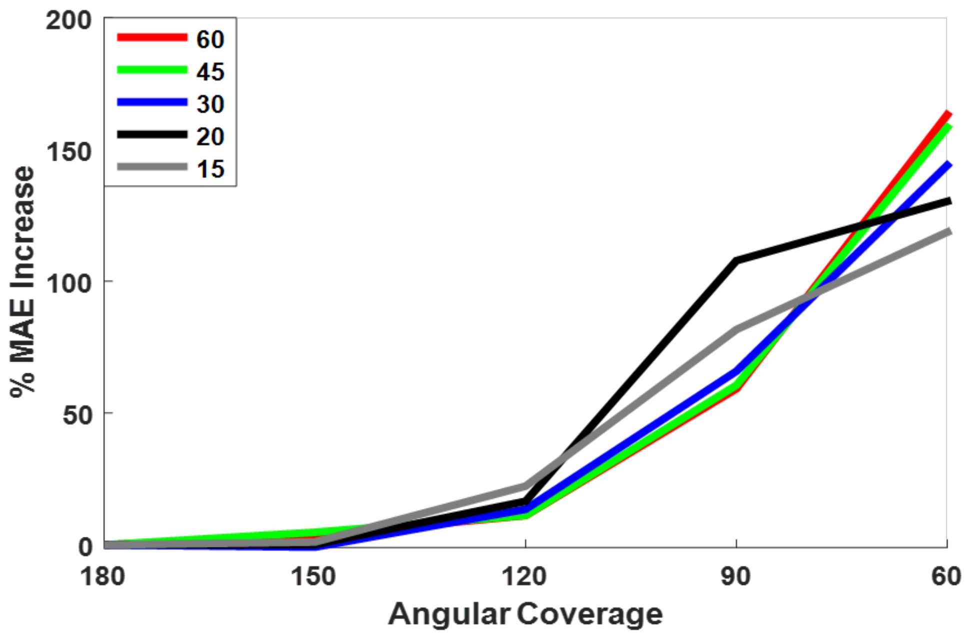

Figure 7.12: Percentage increase of MAE for imaginary part of image as the number of projections is lowered for a fixed coverage. Graphs plotted for different coverages

margins it can handle. So far, in this chapter, reconstructions have been done with 5% noise. However, to see the effect of increasing noise in the data, reconstructions were performed under various levels of noisy data. The effect was observed on reconstruction from 20 views and 120° angular coverage. The effect can be seen in Fig. 7.17 - Fig. 7.18. The reconstruction is good at 10% noise. The real part is still acceptable at 20% noise, however, the imaginary part is considerably degraded. At 50% noise both real and imaginary parts are highly degraded and unacceptable for visual analysis. However, it should be noted that this is too high a noise margin, which should require improvements in the physical acquisition system rather than the reconstruction algorithm itself. In conclusion, it can be inferred that with TV based CS reconstruction, acceptable reconstruction of complex valued objective function can be achieved from moderately noisy data with as limited coverage as 120° and as little measurements as 15 projections. This is a significant feat and highly beneficial in numerous scenarios with either highly limited angular access or various constraints (like available acquisition time) limiting the total number of projections that can be obtained. With an aim to explore other avenues which might also have pertinent effect towards lowering data requirements in tomographic reconstruction, effect of incorporating multiple sparsity promoting factors is briefly explored in the next section.

7.2 Multiple sparse domain incorporation

The fundamental principle behind compressed sensing based signal recovery is to exploit a sparse representation of the signal. If a signal could be represented in multiple sparse

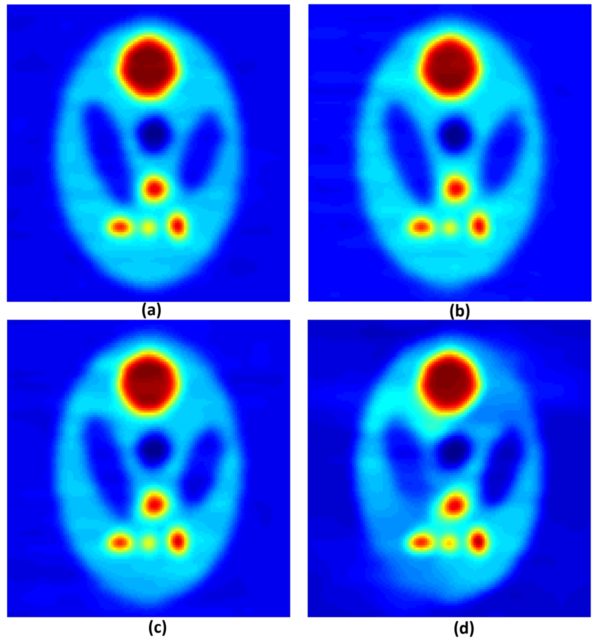

Figure 7.13: Reconstructions of real part of image with 15 views, when real and imaginary parts have similar physical boundaries, for different angular coverage of : (a) 180°, (b) 150°, (c) 120°, and (d) 90°

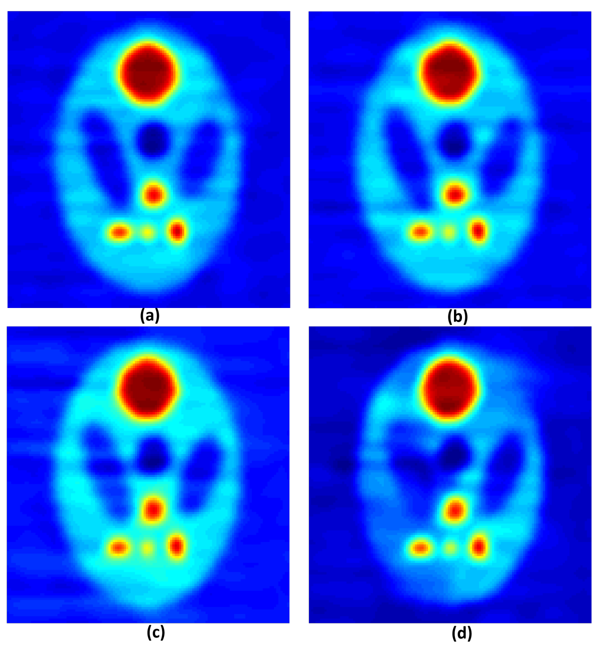

Figure 7.14: Reconstructions of real part of image with 15 views,when real and imaginary parts have similar physical boundaries, for different angular coverage of : (a) 180°, (b) 150°, (c) 120°, and (d) 90°

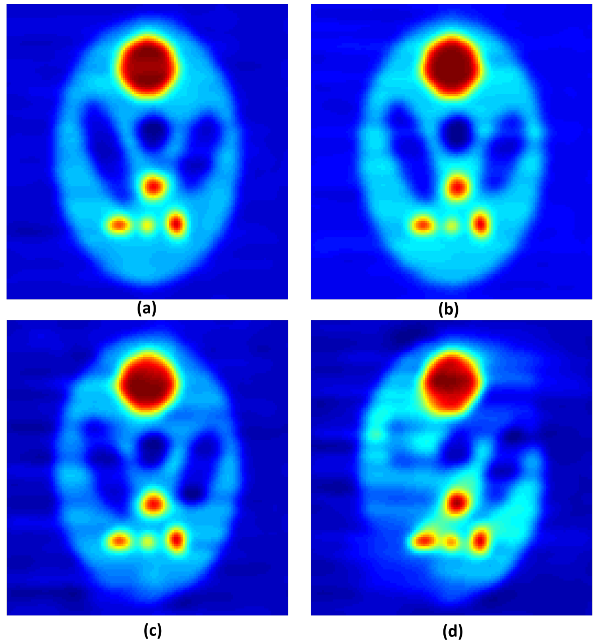

Figure 7.15: Reconstructions of real part of image with 10 views, when real and imaginary parts have similar physical boundaries, for different angular coverage of : (a) 180°, (b) 150°, (c) 120°, and (d) 90°

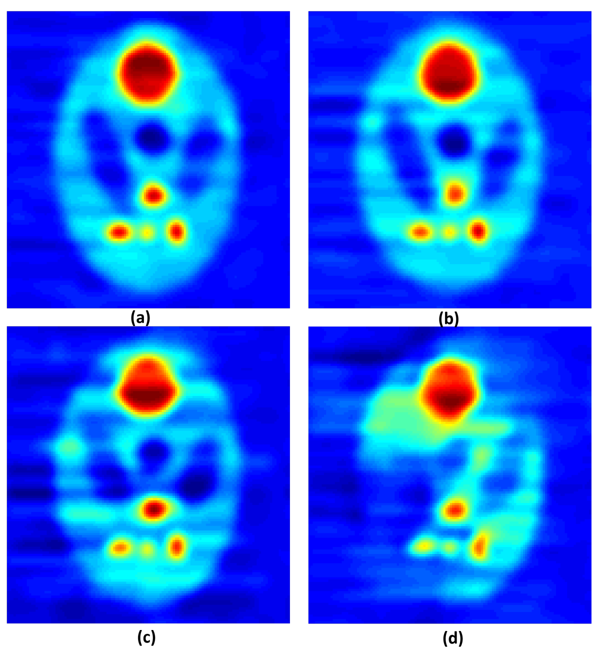

Figure 7.16: Reconstructions of real part of image with 10 views,when real and imaginary parts have similar physical boundaries, for different angular coverage of : (a) 180°, (b) 150°, (c) 120°, and (d) 90°

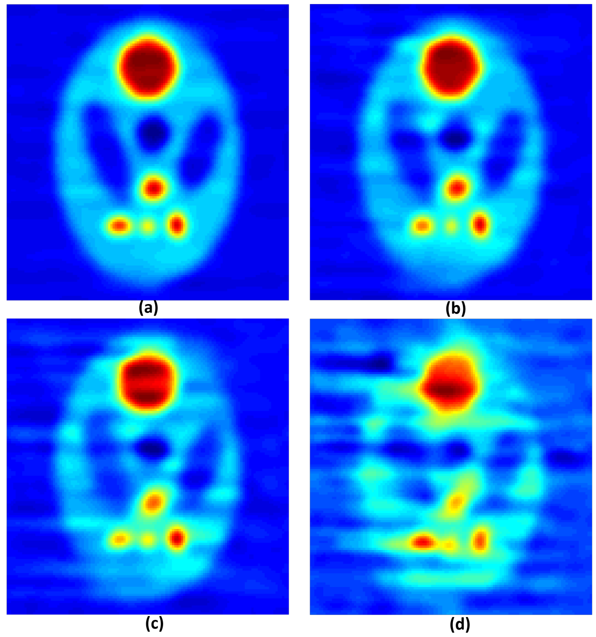

Figure 7.17: Reconstructions of real part of image with 15 views and 120° coverage, when real and imaginary parts have similar physical boundaries, for different noise levels (measured as % of mean signal energy level) : (a) 5%, (b) 10%, (c) 20%, and (d) 50%

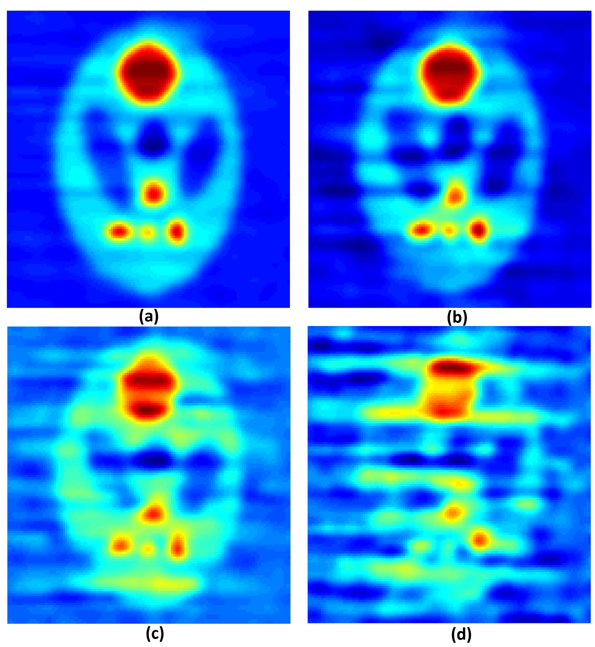

Figure 7.18: Reconstructions of imaginary part of image with 15 views and 120° coverage, when real and imaginary parts have similar physical boundaries, for different noise levels (measured as % of mean signal energy level) : (a) 5%, (b) 10%, (c) 20%, and (d) 50%

domains, it would be interesting to see if these domains could be used simultaneously for better reconstruction. Traditionally wavelets have been a very popular sparse domain in image processing and has been used in CS based reconstructions with great success. It would be instructive to see if wavelets could be incorporated as an added sparse domain in recovery of complex valued objects. If a basic wavelet based penalty term can be incorporated to get a decent level of reconstruction, a vast bank of wavelet (or curvelet, coiflet etc.) based filters open up and provide opportunity of further research towards utilizing multiple sparse representations for increasing reconstruction efficiency or lowering data requirements further. Here a basic wavelet based penalty term has been incorporated using haar wavelets. The main aim is to explore the possibility of incorporating multiple sparse domains easily for complex-valued image reconstruction from sparse data. To incorporate the wavelet sparsity term, the optimization problem of (7.2) is modified as

$$\min_{s} \{G(s) = \| F - \Phi D f_d \|_2^2 + \alpha TV(f_d) + \beta \| \Psi * f_d \|_1\}. \tag{7.3}$$

In the above equation, Ψ is the haar wavelet operator so that $\Psi * f_d$ is the wavelet domain representation of the image f_d. β is the regularization parameter for the second l_1 penalty term. In the following reconstructions, $\alpha = 0.2$ and $\beta = 0.1$ has been used. In Fig. 7.19- Fig. 7.20, reconstruction have been performed by solving the optimization problem (7.3) for 15 projections at different angular coverages.

It is interesting to note that the reconstructions are comparable or marginally better for 180° and 150° coverage but degrades more rapidly than the TV based reconstruction at lower coverage and especially for the imaginary part. There are two possible reasons

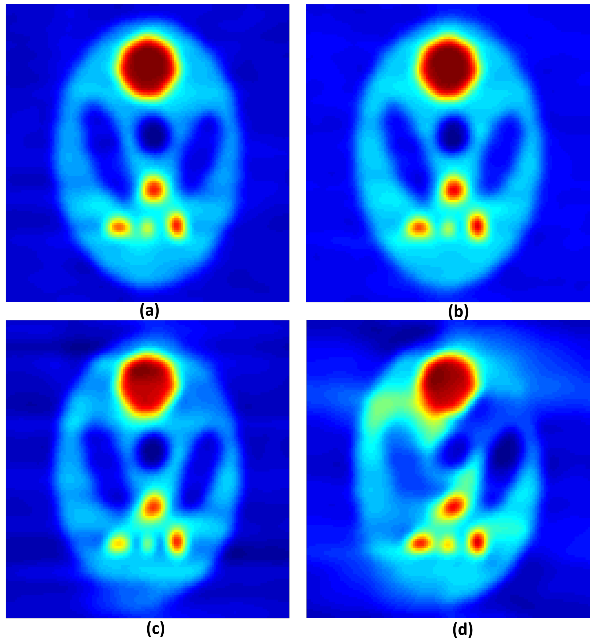

Figure 7.19: Reconstructions of real part of image with 15 views, when real and imaginary parts have similar physical boundaries, for different angular coverage of : (a) 180°, (b) 150°, (c) 120°, and (d) 90°

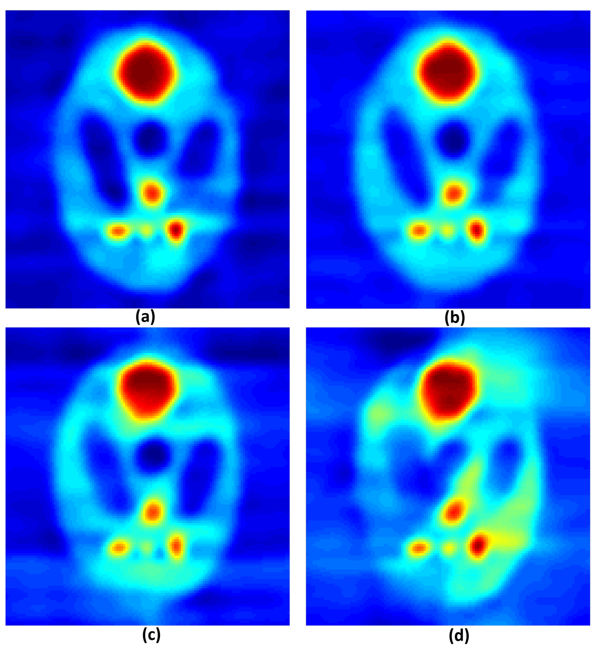

Figure 7.20: Reconstructions of imaginary part of image with 15 views, when real and imaginary parts have similar physical boundaries, for different angular coverage of : (a) 180°, (b) 150°, (c) 120°, and (d) 90°

behind this. Firstly, for theses reconstructions, haar wavelets have been used for wavelet domain representation. This is the simplest wavelet available. Further sophisticated wavelets would actually be much more effective in better sparse representation. Secondly, once a better suited wavelet is determined, the the regularization factors can be optimized to set up a more efficient optimization problem which will generate better reconstructions by truly exploiting the sparsity in multiple domains in parallel. That multiple sparsity promoting terms can be simultaneously used is apparent in these simple exercise. However, there is a huge potential of improvement by using more optimal wavelets than the haar wavelet used here. This is an interesting future work or extension of this research, an avenue to explore with benefits across multiple disciplines.

Chapter 8

Conclusions

8.1 Summary

Diffraction tomography is an active field of study in imaging which is used in nondestructive evaluation and biomedical applications. In many practical scenarios, a major challenge in DT is a limited availability of projection data. The limitations might appear in the form of constraints in angular access or total number of projections or a combination of both. This essentially makes the available set of measurements highly limited or sparse. This thesis focuses on development of efficient methods to handle the challenges on limited data for image reconstruction. Image reconstruction algorithms for diffraction tomography with limited data were investigated and developed. Sparse tomographic reconstruction has been explored under two categories: (a) the moderately limited angular coverage scenario, by exploiting redundancy in projection data and (b) severely limited projection data, both in terms of angular access and number of projections, through employing sparse representations of the test image and invoking compressed sensing framework for image recovery.

8.1.1 Exploiting data redundancy for moderately limited angular diffraction tomography

Traditionally, 360° coverage is required for accurate reconstruction of complex valued object functions. However, under angular coverage range between $180^\circ - 270^\circ$, redundancies are present in the DT projection data. Formulations to exploit these redundancies optimally and in a generalized approach, was shown to provide accurate reconstruction, independent of the image characteristics or features. A novel weighting function for the projection data in its Fourier space was proposed using cumulative distribution functions. Algorithms were developed to reconstruct complex valued images with this weighted projection dataset using filtered backpropagation techniques. This method yielded reconstructions of complex-valued object functions that were shown to be superior to the standard backpropagation algorithm in the coverage range of $[180^\circ - 270^\circ]$. Efficient data-weighting resulted in recovering images from 220° coverage but equivalent to full coverage (360°) reconstruction. Robustness of the algorithms with noisy projection data was also verified.

8.1.2 Compressed Sensing based diffraction tomography from highly sparse data

Reconstruction from highly sparse data with limitations on angular access and number of projections was was developed and evaluated. A compressed sensing framework for DT image reconstruction for complex valued objects has been developed. Using Total Variation as the sparsity norm, accurate reconstruction of complex permittivity distribution was achieved from severely limited projection dataset. Accurate reconstructions from very limited datasets of 15-20 projections with angular access as low as 120° was achieved. Reconstruction from noisy projections established the robustness of the algorithms in presence of noise.

The feasibility of using multiple sparse domains was also explored by adding wavelet domain l_1-norm as an added penalty factor in the optimization problem. A basic Haar wavelet based penalty term was successfully implemented in the optimization scheme to get reconstructions in a CS framework, thereby opening the road to further exploring multiple sparse domain incorporation in the image reconstruction process.

8.2 Contribution: Significance and Benefits

The primary focus of this thesis was to develop reconstruction algorithms to recover complex-valued images under diffraction tomographic regime with varying limitations on the available projection data. In particular, this thesis presents the following contributions:

- Algorithms were developed to exploit redundancy in DT projection data. This is an efficient way to reconstruct complex valued images accurately under moderately limited angular constraints.

- Total variation was successfully employed as a sparsity promoting norm under compressed sensing formulation. The TV algorithm is simple to implement. Using it as the l_1-norm in a CS framework provides an efficient alternative for image recovery. Reconstructions from as few as 15 projection sets and low coverage of 120° has been achieved. The algorithms performed accurately under noisy data proving their robustness to measurement error and related perturbations.

- Use of multiple sparse domains in image recovery was explored briefly. This opens up a huge potential of further research. Optimal exploitation of multiple sparse domains would have applications in scenarios where the availability of projection data is lower than that required in a general CS framework.

The benefits of this research are manifold, the salient ones are:

- The algorithms are applicable for reconstruction of complex valued objective functions or images under the DT regime. This includes modalities such as ultrasonic DT, microwave tomography, ODT etc.
- This research has multi-disciplinary applications such as biomedical imaging, material characterization and structural health monitoring.
- The capability to reconstruct complex valued images is particularly of interest in the present age when smart and artificial materials are increasing in popularity. These are being designed and fabricated for use across a wide gamut of applications. Knowledge of the complex permittivity distribution (or refractive index etc. depending on the application) is fast becoming a necessity for NDE applications and material characterization.

8.3 Future Work

In the first part of the thesis, a generalized approach to exploit data redundancy in DT was presented. The main idea was the introduction of weights based on cumulative distribution functions to the Fourier space projection data. For a given dataset, a single distribution function was used with a fixed set of parameters to exploit redundancy. As an interesting future work, multiple parameter sets can be employed based on frequency locations. An optimization problem can be set up to determine parameter sets based on a particular ν_m in Fig. 3.1(d). This can enable application of independent and different cdfs for each value of ν_m and can lead to further image improvements in the lower limits of operation below 220° angular coverage.

In the second part of the thesis, DT reconstruction under a CS framework was performed to recover complex valued images. In case of medical imaging, TV had been successfully used as a regularization parameter for sparse reconstructions. So in a compressed sensing based setup, employing TV as the l_1 norm where the gradient magnitude is a sparse representation of the image is a natural choice and implementation of the method has been demonstrated. Outside TV, wavelets in general have found great success in image compression and recovery. As can be expected, different applications might find different forms of sparse representations. As a result, the sparsity promoting l_1 norm would also have to be changed. For specific applications, finding the most effective sparse domains is an interesting and important research goal. This could be studied under the next phase of this research. Generalized methods to extract most effective sparse domains for complex-valued reconstruction would be of value across multiple disciplines. As an example, in this research, Haar wavelets have been used to demonstrate a basic platform for using multiple sparsity promoting norms in the minimizing term of the optimization problem. Numerous wavelets and filter databases are available today which can be broadly classified into a few standard categories. It is logical to assume that the most effective wavelet category would actually be determined by the type of application being developed and can be determined through investigation into the nature of the data features associated with the problem at hand. Thus a procedure to select optimum wavelets or filters based on the associated application would be an interesting avenue to explore with benefits across multiple disciplines.

APPENDICES

Appendix A

Distribution Function based weight generation

Gamma-cdf based weighting:

The gamma-cdf is defined as $F(x) = \int_{-\infty}^{x} f(t)dt$, where f is the gamma probability density function defined as:

$$f(t|a,b) = \begin{cases} \frac{1}{\Gamma(a)b^a} t^{a-1} e^{-t/b}, & t \geq 0, \\ 0, & t < 0. \end{cases} \tag{A.1}$$

where $a > 0$ and $b > 0$ are parameters, and $\Gamma(a) = \int_0^\infty t^{a-1} e^{-t} dt$ is standard gamma-function. As we can see that gamma-cdf has support on $[0, \infty)$, $F(2\alpha + \pi/2) < 1$, which does not meet (3.5). Therefore weights created using gamma-cdf in its original form will be discontinuous at the boundary between A and B, and consequently at the boundary between B and C of Fig. 3.1(d). One possible way to get a continuos weight is by inputting a transformed argument. So for fixed $\nu_m \in [-\nu_0, \nu_0]$, we shall construct weights by using

$$w(\nu_m, \phi) = F\left(\tan\left(\frac{\pi}{2}\frac{\phi}{2\alpha + \pi/2}\right)\right), \tag{A.2}$$

where F is the gamma-cdf as defined above.

Normal-cdf based weighting:

In case of normal-cdf, we used truncation method as follows:

$$w(\nu_m, \phi) = \frac{F(\nu_m|\mu, \sigma) - F(0|\mu, \sigma)}{F(2\alpha + \pi/2|\mu, \sigma) - F(0|\mu, \sigma)}, \tag{A.3}$$

where $\mu \in (-\infty, \infty)$ and $\sigma > 0$ are parameters and

$$F(x|\mu, \sigma) = \frac{1}{\sqrt{2\pi}\sigma} \int_{-\infty}^{x} e^{-(t-\mu)^2/2\sigma^2} dt. \tag{A.4}$$

Appendix B

Non-linear Optimization Techniques

When we have an under-determined system, i.e. the number of unknowns is more than the number of measurements, there is generally no unique solution. A typical example would be the projection data from a limited angle ($\ll 360^o\circ$) tomography experiment. The general approach to solving this type of systems is to find an 'optimal' solution from the set of all probable solutions while obeying some constraints. These constraints are either known a priori or known through experiment (i.e. measured data). This solution is approximate and is reached through a series of steps or iterations which aim to minimize a 'cost function' or 'objective function'. This approach of reaching the most acceptable but approximate solution forms the branch of computational science called optimization. In our case, when tomographic image reconstruction is done from limited number of projection data, iterative techniques are used which employ some form of optimization. Thus this chapter is a brief note on optimization and some of the non-linear optimization techniques used in this research. Consider a simple system of the form

$$Ax = b. \tag{B.1}$$

If x^* be an approximate solution to the problem, then often the corresponding *residual* is defined as $Ax^* - b$. The aim would be to minimize this residual. The ideal solution would produce a zero residual. Let this residual be expressed as $f(x) = Ax - b$. In this case, the cost function (without any other constraints) would be the residual and we have the minimization problem as

$$\min_x f(x). \tag{B.2}$$

Based on the characteristics and complexity of the system represented by A, this minimization problem could be anything from a simple linear to highly non-linear system. For many practical scenarios, incorporating all the requirements into this objective function creates a complex function which needs to be minimized while conforming to the 'known' or experimental datapoints.

Linear systems:

Traditionally, a system is said to be linear if it obeys additivity (superposition) and scalar multiplication (homogeneity). Mathematically, a function can be expressed in a general form as

$$f(\alpha x) = \alpha f(x), \quad f(x+y) = f(x) + f(y) \tag{B.3}$$

here f represents a general function or operator. If a system however complex, obeys linearity, it can then be broken into a sum of many smaller and relatively simpler units. A very complex problem can then be decomposed into an aggregate of smaller tractable problems and solved independently. Thus it is always convenient if a system can be modeled in a linear fashion.

Beyond linearity:

Many complex real world problems are inherently non-linear and cannot be expressed through linear approximations. As a result, non-linear mathematical theories have seen tremendous growth over the last few decades. Several branches of mathematics e.g. fractal theory, non-linear dynamics, chaos etc. have been developed. These tools in turn have helped the development of new theories in pure and applied sciences. These developments coupled with the advent of powerful computers with high computational capabilities led to the development of many methods to tackle real-world problems. Nonlinear optimization is one of the foremost techniques. An optimization problem is generally formulated as:

$$\min_{x} \quad f(x), \quad s.t. \quad g_1(x) = 0, \quad g_2(x) = 0...., \quad g_n(x) \geq 0 \tag{B.4}$$

.

Here, f is a scalar valued function which is being minimized subject to the constraint equations and inequalities: g_1, g_2 etc. The presence of these constraints in effect incorporate *a priori* information and thereby limit the search space. This type of optimization is called constrained optimization and is of fundamental importance in reconstruction techniques. If the constraints are not present, then the procedure is termed unconstrained optimization. Optimization is a process of finding an amenable solution from the feasible space. Based on the search approach, optimization methods can be classified into direct and indirect methods. The former enumerate the possible solutions and evaluate the object function for all sets to determine the best solution set. Common direct methods include exhaustive search, the simplex method, random method, the Fibonacci search and more. A complete treatment can be found in standard texts, [70], [71] etc. However, direct methods are only efficient when there are small number of variables or in cases with countable inputs. For continuous problems with complicated object functions, the implementation of these methods is unpractical. In the last few decades, the genetic algorithms became an efficient member of direct optimization methods. This searching process exploited analogous concepts of gene mutations of organisms to select smaller populations for evaluating the objective function. This results in highly improved efficiency of direct search process. It has been applied to many real world datasets including microwave imaging. Indirect methods mostly involve gradient based techniques in principle. If analytical forms of the objective function exist, then the optimization steps are iteratively directed using the gradient information. The popular methods under this category include the steepest descent (SD) method, Gauss-Newton (GN) method, conjugate gradient (CG) method, Levenberg-Marquardt (LM) method etc. The simplest among these is possibly the steepest descent method whereas the method of conjugate gradients is one of the mostly used across multiple disciplines because of it versatility and quick convergence. In this work, both SD and CG methods have been used at different phases and hence they are briefly described below. The theory and explanations have mostly been summarized from [70] and [72]

Steepest Descent Method

One of the very well established methods, the steepest descent method uses the negative direction of gradient vector as the direction of minimization. Intuitively and geometrically it makes sense. The gradient gives the direction of maximum increase of the function. The negative gradient is the opposite direction and hence the direction where the fuction will be minimized. The method starts with an initial trial point X_i and iteratively moves along the steepest descent directions till an optimum point or convergence is reached. the algorithm consists of the following steps:

1. Start with an arbitrary initial point X_i. Set iteration number i=1.

2. Find steepest descent direction as: $S_i = -\nabla f_i = -\nabla f(X_i)$.

3. Find the optimal step length λ_i^*: $\frac{\partial f}{\partial \lambda} |_{\lambda=\lambda^*} = 0$

4. Set $X_{i+1} = X_i + \lambda^* S_i$.

5. Check X_{i+1} for optimality. If so, iteration is stopped, otherwise the loop is iterated till convergence is reached.

Convergence: The stopping criteria of any design problem depends on the problem itself and the design requirements. The iterations are stopped when either any or a combination of the stopping criteria are fulfilled. Some typical stopping criteria could be:

1. The change in functional value between successive steps is small: $\left| \frac{f(X_{i+1})-f(X_i)}{f(X_i)} \right| \leq \epsilon_1$

2. When change in the design vector between successive steps is small: $|X_{i+1} - X_i| \leq \epsilon_2$

3. When partial derivatives of the minimizing functional are small.

4. The maximum number of allowed iterations is reached.

Conjugate Gradient Method

Steepest descent is a very simple, fast and easy to implement algorithm. It has found success in a lot of applications. However, it is not a very fast algorithm and it can get trapped in a local minimum. Another popular and robust technique which has been of great importance in the field of optimization is the method of conjugate gradients. It extends the method of steepest descent with great improvements. The fundamental principle behind this method is the use of 'conjugate directions'. This ensures that the method will be quadratically convergent. This is very beneficial as it implies that the convergence will be reached in n steps or less.

Conjugate Directions: A conjugate directions method can minimize a quadratic function within a finite number of iterations. Any general non-linear function can be well approximated near its optimum point by a quadratic. So any quadratically convergent method should be able to achieve a quicker convergence for general non-linear functions.

Definition- If A be an $n \times n$ symmetric matrix, the set of n vectors $\{S_i\}$ is said to be conjugate with respect to A if $S_i^T \mathrm{A} S_j = 0$, for all $i \neq j, i = 1, 2, ..., n, j = 1, 2, ..., n$

Orthogonal directions or unit vectors for cartesian co-ordinate systems would be a specific case of conjugate directions with A = I. S is a set of n linearly independent vectors and so they can form a basis, i.e. any vector X can be expressed as a linear combination of the elements of S. Let us assume that we need to solve for the system $Ax = b$. Let X_0 be the initial starting solution and X^* be the true solution. The difference can also be expressed in terms of S, i.e.:

$$X^* - X_0 = \sum_{j=0}^{n-1} \alpha_j S_j \tag{B.5}$$

Multiplying both sides by $S_k^T A$, on the left hand side we have

$$S_k^T A(X^* - X_0) = S_k^T (b - Ax_0) = S_k^T r_0$$

and on the right hand side we have

$$S_k^T A \sum_{j=0}^{n-1} \alpha_j S_j = \alpha_k S_k^T A S_k.$$

and hence,we can get

$$\alpha_k = \frac{S_k^T r_0}{S_k^T A S_k}. \tag{B.6}$$

Then we can have an algorithm to solve $AX^* = b$:

1. Pick X_k and A-conjugate directions S_k. Set iteration number $k = 1$
2. Set $\alpha_k = \frac{S_k^T r_0}{S_k^T A S_k}$.
3. Set $X_{k+1} = X_k + \alpha_k S_k$.
4. Continue for n-iterations.

After n steps, then we should have $X_n = X^*$.

The process to generate a set of A-conjugate vectors is not too complex. It can be done by starting with any set of linearly independent vectors $V = V_k$ and then applying a Gram-Schmidt transformation with respect to A. A standard stable numerical approach is the following:

1. Let $S = V$.

2. Then, compute $\forall k, S_{k+1} = S_{k+1} - \sum_{j=1}^{k} \frac{S_k^T A S_{k+1}}{S_j^T A S_j} S_j$

The **conjugate gradient** method is a special case of the method of conjugate directions. Here the calculation of X at each stage is interlaced with the calculation of the new S_k vector. The algorithm can be applied through these steps:

1. Let X_1 be the initial guess. Let $r_1 = b - AX_1$ and $S_1 = r_1$.

2. For k=1,2,.. until convergence,

(a) Compute search parameter α_k, the new iterate and residual

$$\alpha_k = \frac{S_k^T r_k}{S_k^T A S_k}$$

$$X_{k+1} = X_k + \alpha_k S_k$$

$$r_{k+1} = r_k - \alpha_k A S_k$$

(b) Compute the new search direction

$$\beta_k = -\frac{S_k^T A r_{k+1}}{S_k^T A S_k}$$

$$S_{k+1} = r_{k+1} + \beta_k \S_k$$

After $K \leq n$ steps, the algorithm terminates with $r_K = 0$ and $X_K = X^*$. Since the direction S_k used here are A-conjugate, the process should converge for quadratic functions in n-cycles or less. But for ill-conditioned quadratics, the method may require more cycles for convergence. However, this method is superior to the steepest descent method in terms of faster convergence and lower error bounds. This algorithms has been researched and implemented on on a variety of problems. As a result many readily available CG-codes can be directly incorporated into reconstruction algorithms. The CG iterations are suitable for incorporating into TV minimization for image reconstruction. To compute the CG iterations the gradient of the TV term has to be computed as well. In the expression for TV in (7.1), to avoid a zero denominator in the TV term, an approximation which is often employed is: $\| D_{n_1,n_2} f_d \| \approx \sqrt{(D^h_{n_1,n_2}\ f_d)^2 + (D^v_{n_1,n_2}\ f_d)^2 + \mu}$, where μ is a small positive number. It can further be approximated as:

$$\begin{aligned}\nabla \| D_{n_1,n_2}\ f_d \|_2 = {} & \frac{D^h_{n_1,n_2}\ f_d}{\| D_{n_1,n_2}\ f_d \|_2} + \frac{D^v_{n_1,n_2}\ f_d}{\| D_{n_1,n_2}\ f_d \|_2} \\ & - \frac{D^h_{n_1,n_2-1}\ f_d}{\| D_{n_1,n_2-1}\ f_d \|_2} - \frac{D^v_{n_1-1,n_2}\ f_d}{\| D_{n_1-1,n_2}\ f_d \|_2}.\end{aligned} \tag{B.7}$$

BIBLIOGRAPHY

BIBLIOGRAPHY

[1] R. G. Baraniuk, “Compressive sensing,” *IEEE signal processing magazine*, vol. 24, no. 4, 2007.

[2] A. Devaney, “A filtered backpropagation algorithm for diffraction tomography,” *Ultrasonic imaging*, vol. 4, no. 4, pp. 336–350, 1982.

[3] A. C. Kak and M. Slaney, *Principles of computerized tomographic imaging.* Society for Industrial and Applied Mathematics, 2001.

[4] W. Tabbara, B. Duchêne, C. Pichot, D. Lesselier, L. Chommeloux, and N. Joachimowicz, “Diffraction tomography: contribution to the analysis of some applications in microwaves and ultrasonics,” *Inverse Problems*, vol. 4, no. 2, p. 305, 1988.

[5] G. S. Kino, “Acoustic imaging for nondestructive evaluation,” *Proceedings of the IEEE*, vol. 67, no. 4, pp. 510–525, 1979.

[6] B. Duchêne, D. Lesselier, and W. Tabbara, “Experimental investigation of a diffraction tomography technique in fluid ultrasonics,” *Ultrasonics, Ferroelectrics, and Frequency Control, IEEE Transactions on*, vol. 35, no. 4, pp. 437–444, 1988.

[7] S. Semenov, “Microwave tomography: review of the progress towards clinical applications,” *Philosophical Transactions of the Royal Society of London A: Mathematical, Physical and Engineering Sciences*, vol. 367, no. 1900, pp. 3021–3042, 2009.

[8] A. Devaney, “Geophysical diffraction tomography,” *Geoscience and Remote Sensing, IEEE Transactions on*, no. 1, pp. 3–13, 1984.

[9] E. Robinson, “Image reconstruction in exploration geophysics,” University of Tulsa, Tulsa, OK, Tech. Rep., 1984.

[10] E. V. Malyarenko and M. K. Hinders, “Ultrasonic lamb wave diffraction tomography,” *Ultrasonics*, vol. 39, no. 4, pp. 269–281, 2001.

[11] M. H. Ritzwoller, N. M. Shapiro, M. P. Barmin, and A. L. Levshin, “Global surface wave diffraction tomography,” *Journal of Geophysical Research: Solid Earth (1978–2012)*, vol. 107, no. B12, pp. ESE–4, 2002.

[12] P. Guo and A. J. Devaney, "Comparison of reconstruction algorithms for optical diffraction tomography," *JOSA A*, vol. 22, no. 11, pp. 2338–2347, 2005.

[13] T. C. Wedberg and J. J. Stamnes, "Experimental examination of the quantitative imaging properties of optical diffraction tomography," *JOSA A*, vol. 12, no. 3, pp. 493–500, 1995.

[14] T. Wedberg and W. Wedberg, "Tomographic reconstruction of the cross-sectional refractive index distribution in semi-transparent, birefringent fibres," *Journal of Microscopy*, vol. 177, no. 1, pp. 53–67, 1995.

[15] W. Gorski and W. Osten, "Tomographic imaging of photonic crystal fibers," *Optics letters*, vol. 32, no. 14, pp. 1977–1979, 2007.

[16] J. Y. Cheng and A. J. Devaney, "Inverse scattering and diffraction tomography in cylindrical background media," *JOSA A*, vol. 23, no. 5, pp. 1038–1047, 2006.

[17] Y. Sung, W. Choi, C. Fang-Yen, K. Badizadegan, R. R. Dasari, and M. S. Feld, "Optical diffraction tomography for high resolution live cell imaging," *Optics express*, vol. 17, no. 1, pp. 266–277, 2009.

[18] J. Kostencka, T. Kozacki, A. Kuś, and M. Kujawińska, "Accurate approach to capillary-supported optical diffraction tomography," *Optics express*, vol. 23, no. 6, pp. 7908–7923, 2015.

[19] I. Catapano, L. Di Donato, L. Crocco, O. M. Bucci, A. F. Morabito, T. Isernia, and R. Massa, "On quantitative microwave tomography of female breast," *Progress In Electromagnetics Research*, vol. 97, pp. 75–93, 2009.

[20] D. G. Drogoudis, G. A. Kyriacou, and J. N. Sahalos, "Microwave tomography employing an adjoint network based sensitivity matrix," *Progress In Electromagnetics Research*, vol. 94, pp. 213–242, 2009.

[21] A. Baran, D. J. Kurrant, A. Zakaria, E. C. Fear, and J. LoVetri, "Breast imaging using microwave tomography with radar-based tissue-regions estimation," *Progress In Electromagnetics Research*, vol. 149, pp. 161–171, 2014.

[22] N. Bayat and P. Mojabi, "The effect of antenna incident field distribution on microwave tomography reconstruction," *Progress In Electromagnetics Research*, vol. 145, pp. 153–161, 2014.

[23] X. Ren, X. Yin, R. Yang, and W. Yu, "A three-dimensional imaging algorithm for tomography sar," in *Geoscience and Remote Sensing Symposium, 2009 IEEE International, IGARSS 2009*, vol. 3. IEEE, 2009, pp. III–184.

[24] X.-Z. Ren, L. H. Qiao, and Y. Qin, "A three-dimensional imaging algorithm for tomography sar based on improved interpolated array transform1," *Progress In Electromagnetics Research*, vol. 120, pp. 181–193, 2011.

[25] A. Capozzoli, C. Curcio, and A. Liseno, "Fast gpu-based interpolation for sar backprojection," *Progress In Electromagnetics Research*, vol. 133, pp. 259–283, 2013.

[26] G. Tsihrintzis, A. J. Devaney *et al.*, "Higher-order (nonlinear) diffraction tomography: reconstruction algorithms and computer simulation," *Image Processing, IEEE Transactions on*, vol. 9, no. 9, pp. 1560–1572, 2000.

[27] A. T. Vouldis, C. N. Kechribaris, T. Maniatis, K. S. Nikita, N. K. Uzunoglu *et al.*, "Three-dimensional diffraction tomography using filtered backpropagation and multiple illumination planes," *Instrumentation and Measurement, IEEE Transactions on*, vol. 55, no. 6, pp. 1975–1984, 2006.

[28] A. Devaney, "A computer simulation study of diffraction tomography," *Biomedical Engineering, IEEE Transactions on*, no. 7, pp. 377–386, 1983.

[29] S. Pan and A. C. Kak, "A computational study of reconstruction algorithms for diffraction tomography: interpolation versus filtered-backpropagation," *Acoustics, Speech and Signal Processing, IEEE Transactions on*, vol. 31, no. 5, pp. 1262–1275, 1983.

[30] X. Pan and M. A. Anastasio, "Minimal-scan filtered backpropagation algorithms for diffraction tomography," *JOSA A*, vol. 16, no. 12, pp. 2896–2903, 1999.

[31] A. J. Devaney, "The limited-view problem in diffraction tomography," *Inverse problems*, vol. 5, no. 4, p. 501, 1989.

[32] S. J. LaRoque, E. Y. Sidky, and X. Pan, "Accurate image reconstruction from few-view and limited-angle data in diffraction tomography," *JOSA A*, vol. 25, no. 7, pp. 1772–1782, 2008.

[33] H. Ayasso, B. Duchêne, and A. Mohammad-Djafari, "Bayesian inversion for optical diffraction tomography," *Journal of Modern Optics*, vol. 57, no. 9, pp. 765–776, 2010.

[34] Y. Sung and R. R. Dasari, "Deterministic regularization of three-dimensional optical diffraction tomography," *JOSA A*, vol. 28, no. 8, pp. 1554–1561, 2011.

[35] M. A. Anastasio and X. Pan, "Full-and minimal-scan reconstruction algorithms for fan-beam diffraction tomography," *Applied optics*, vol. 40, no. 20, pp. 3334–3345, 2001.

[36] X. Pan, M. Anastasio *et al.*, "On a limited-view reconstruction problem in diffraction tomography," *Medical Imaging, IEEE Transactions on*, vol. 21, no. 4, pp. 413–416, 2002.

[37] X. Pan, "Unified reconstruction theory for diffraction tomography, with consideration of noise control," *JOSA A*, vol. 15, no. 9, pp. 2312–2326, 1998.

[38] P. Paladhi, A. Sinha, A. Tayebi, L. Udpa, and A. Tamburrino, "Data redundancy in diffraction tomography," in *Applied Computational Electromagnetics (ACES), 2015 31st International Review of Progress in*, March 2015, pp. 1–2.

[39] G. A. Tsihrintzis and A. J. Devaney, "Stochastic diffraction tomography: Theory and computer simulation," *Signal processing*, vol. 30, no. 1, pp. 49–64, 1993.

[40] M. A. Anastasio and X. Pan, "Investigation of the noise properties of a new class of reconstruction methods in diffraction tomography," *International Journal of Imaging Systems and Technology*, vol. 10, no. 6, pp. 437–445, 1999.

[41] E. J. Candè and M. B. Wakin, "An introduction to compressive sampling," *Signal Processing Magazine, IEEE*, vol. 25, no. 2, pp. 21–30, 2008.

[42] E. Candes and J. Romberg, "Sparsity and incoherence in compressive sampling," *Inverse problems*, vol. 23, no. 3, p. 969, 2007.

[43] D. L. Donoho, "Compressed sensing," *Information Theory, IEEE Transactions on*, vol. 52, no. 4, pp. 1289–1306, 2006.

[44] C. E. Shannon, "A mathematical theory of communication," *ACM SIGMOBILE Mobile Computing and Communications Review*, vol. 5, no. 1, pp. 3–55, 2001.

[45] E. J. Candès, J. Romberg, and T. Tao, "Robust uncertainty principles: Exact signal reconstruction from highly incomplete frequency information," *Information Theory, IEEE Transactions on*, vol. 52, no. 2, pp. 489–509, 2006.

[46] E. J. Candes, J. K. Romberg, and T. Tao, "Stable signal recovery from incomplete and inaccurate measurements," *Communications on pure and applied mathematics*, vol. 59, no. 8, pp. 1207–1223, 2006.

[47] E. J. Candes and T. Tao, "Near-optimal signal recovery from random projections: Universal encoding strategies?" *Information Theory, IEEE Transactions on*, vol. 52, no. 12, pp. 5406–5425, 2006.

[48] M. F. Duarte, M. A. Davenport, D. Takhar, J. N. Laska, T. Sun, K. E. Kelly, R. G. Baraniuk *et al.*, "Single-pixel imaging via compressive sampling," *IEEE Signal Processing Magazine*, vol. 25, no. 2, p. 83, 2008.

[49] M. Mishali and Y. C. Eldar, "From theory to practice: Sub-nyquist sampling of sparse wideband analog signals," *Selected Topics in Signal Processing, IEEE Journal of*, vol. 4, no. 2, pp. 375–391, 2010.

[50] M. Lustig, D. Donoho, and J. M. Pauly, "Sparse mri: The application of compressed sensing for rapid mr imaging," *Magnetic resonance in medicine*, vol. 58, no. 6, pp. 1182–1195, 2007.

[51] H. Jung, K. Sung, K. S. Nayak, E. Y. Kim, and J. C. Ye, "k-t focuss: A general compressed sensing framework for high resolution dynamic mri," *Magnetic Resonance in Medicine*, vol. 61, no. 1, pp. 103–116, 2009. [Online]. Available: http://dx.doi.org/10.1002/mrm.21757

[52] M. Lustig, D. Donoho, J. Santos, and J. Pauly, "Compressed sensing mri," *Signal Processing Magazine, IEEE*, vol. 25, no. 2, pp. 72–82, March 2008.

[53] R. Chartrand, "Fast algorithms for nonconvex compressive sensing: Mri reconstruction from very few data," in *Biomedical Imaging: From Nano to Macro, 2009. ISBI'09. IEEE International Symposium on.* IEEE, 2009, pp. 262–265.

[54] U. Gamper, P. Boesiger, and S. Kozerke, "Compressed sensing in dynamic mri," *Magnetic Resonance in Medicine*, vol. 59, no. 2, pp. 365–373, 2008.

[55] H. Jung, K. Sung, K. S. Nayak, E. Y. Kim, and J. C. Ye, "k-t focuss: A general compressed sensing framework for high resolution dynamic mri," *Magnetic Resonance in Medicine*, vol. 61, no. 1, pp. 103–116, 2009.

[56] K. Choi, J. Wang, L. Zhu, T.-S. Suh, S. Boyd, and L. Xing, "Compressed sensing based cone-beam computed tomography reconstruction with a first-order methoda)," *Medical physics*, vol. 37, no. 9, pp. 5113–5125, 2010.

[57] Z. Zhu, K. Wahid, P. Babyn, D. Cooper, I. Pratt, and Y. Carter, "Improved compressed sensing-based algorithm for sparse-view ct image reconstruction," *Computational and mathematical methods in medicine*, vol. 2013, 2013.

[58] H. Yu and G. Wang, "Compressed sensing based interior tomography," *Physics in medicine and biology*, vol. 54, no. 9, p. 2791, 2009.

[59] J. Provost and F. Lesage, "The application of compressed sensing for photo-acoustic tomography," *Medical Imaging, IEEE Transactions on*, vol. 28, no. 4, pp. 585–594, 2009.

[60] A. Hanif, A. Mansoor, and T. Ejaz, "Iterative tomographic image reconstruction by compressive sampling," in *Image Processing (ICIP), 2010 17th IEEE International Conference on*, Sept 2010, pp. 4313–4316.

[61] S. Mallat, *A wavelet tour of signal processing: the sparse way.* Academic press, 2008.

[62] G. Strang, "The discrete cosine transform," *SIAM review*, vol. 41, no. 1, pp. 135–147, 1999.

[63] E. J. Candes and T. Tao, "Decoding by linear programming," *Information Theory, IEEE Transactions on*, vol. 51, no. 12, pp. 4203–4215, 2005.

[64] D. Baron, M. F. Duarte, M. B. Wakin, S. Sarvotham, and R. G. Baraniuk, "Distributed compressive sensing," *CoRR*, vol. abs/0901.3403, 2009. [Online]. Available: http://arxiv.org/abs/0901.3403

[65] S. Boyd and L. Vandenberghe, *Convex optimization.* Cambridge university press, 2004.

[66] S. Hua, M. Ding, and M. Yuchi, "Sparse-view ultrasound diffraction tomography using compressed sensing with nonuniform fft," *Computational and mathematical methods in medicine*, vol. 2014, 2014.

[67] M. M. Bronstein, A. M. Bronstein, M. Zibulevsky, and H. Azhari, "Reconstruction in diffraction ultrasound tomography using nonuniform fft," *Medical Imaging, IEEE Transactions on*, vol. 21, no. 11, pp. 1395–1401, 2002.

[68] L. Liberti and N. Maculan, *Global optimization: from theory to implementation*. Springer Science & Business Media, 2006, vol. 84.

[69] J. F. Sturm, "Using sedumi 1.02, a matlab toolbox for optimization over symmetric cones," *Optimization methods and software*, vol. 11, no. 1-4, pp. 625–653, 1999.

[70] S. S. Rao, *Engineering optimization: theory and practice*. John Wiley & Sons, 1996.

[71] K. Deb, *Optimization for engineering design: Algorithms and examples*. PHI Learning Pvt. Ltd., 2012.

[72] Y. Saad, *Iterative methods for sparse linear systems*. Siam, 2003.